J. Fluid Mech. (2019), *vol.* 863, *pp.* 513–544.
doi:10.1017/jfm.2018.1014

Tracking vortex surfaces frozen in the virtual velocity in non-ideal flows

Jinhua Hao[1], **Shiying Xiong**[1] **and Yue Yang**[1,2,†]

[1]State Key Laboratory for Turbulence and Complex Systems, College of Engineering, Peking University, Beijing 100871, China

[2]CAPT and BIC-ESAT, Peking University, Beijing 100871, China

(Received 24 July 2018; revised 13 October 2018; accepted 6 December 2018; first published online 25 January 2019)

We demonstrate that, if a globally smooth virtual circulation-preserving velocity exists, Kelvin's and Helmholtz's theorems can be extended to some non-ideal flows which are viscous, baroclinic or with non-conservative body forces. Then we track vortex surfaces frozen in the virtual velocity in the non-ideal flows, based on the evolution of a vortex-surface field (VSF). For a flow with a viscous-like diffusion term normal to the vorticity, we obtain an explicit virtual velocity to accurately track vortex surfaces in time. This modified flow is dissipative but prohibits reconnection of vortex lines. If a globally smooth virtual velocity does not exist, an approximate virtual velocity can still facilitate the tracking of vortex surfaces in non-ideal flows. In a magnetohydrodynamic Taylor–Green flow, we find that the conservation of vorticity flux is significantly improved in the VSF evolution convected by the approximate virtual velocity instead of the physical velocity, and the spurious vortex deformation induced by the Lorentz force is eliminated.

Key words: topological fluid dynamics, vortex dynamics

1. Introduction

The ideal fluid flow, i.e. a strictly inviscid barotropic flow with conservative body forces, has multiple conservation laws for vorticity and related quantities, e.g. Kelvin's circulation theorem (Thompson 1869), Helmholtz's vorticity theorem (Helmholtz 1858), Ertel's theorem for potential vorticity (Ertel 1942) and the conservation of helicity (Moreau 1961; Moffatt 1969). In particular, Helmholtz's theorem implies that vortex lines and surfaces are frozen in ideal flows, so we can exactly track them in time from a Lagrangian view.

Most real flows, however, can be viscous, baroclinic or with non-conservative body forces, so the vorticity-related conservation theorems break down in reality (see Kida & Takaoka 1991; Chen *et al.* 2006). The breakdown of Helmholtz's theorem implies that we cannot exactly track vortex lines and surfaces along the velocity field. It appears to be a major obstacle for developing the Lagrangian formulation for non-ideal real flows and understanding the 'abrupt and mysterious' structural evolution in transitional flows (see Mullin 2011).

† Email address for correspondence: yyg@pku.edu.cn

The breakdown of vorticity-related conservation theorems causes a formidable gap between the vortex dynamics of ideal and real fluid flows in particular, or between Euler and Navier–Stokes (NS) equations in general. In ideal flows, the topology of vortex lines is invariant in time provided that persistent stretching of vortex lines does not form a finite-time singularity (e.g. Kerr 1993; Majda & Bertozzi 2001; Hou & Li 2007). In real flows, however, topological changes of vortex lines can occur from vortex reconnection (see Kida & Takaoka 1994), and turbulence can be generated from initially laminar flows with small perturbations through a transitional process.

There have been a few attempts to extend the vorticity-related conservation theorems to non-ideal flows. The basic idea is to construct a 'virtual velocity' and reformulate the momentum or vorticity equation in an advection form driven by the virtual velocity. Furthermore, as an analogy between ideal and non-ideal flows in hydrodynamic (HD) flows, a similar extension based on the virtual velocity can be applied to magnetohydrodynamic (MHD) flows, e.g. extending Alfvén's theorem for the magnetic field in ideal MHD flows (Alfvén 1943) to resistive MHD flows.

The virtual velocity may be referred to by various names in the literature. Newcomb (1958) proposed a 'flux-preserving' velocity for a magnetic field in conducting flows, and demonstrated that, conceptually, the magnetic flux of magnetic field lines convected by the flux-preserving velocity can be conserved in non-ideal MHD flows (see Priest & Forbes 2000). Constantin & Iyer (2008) derived a probabilistic representation of the NS equations based on stochastic Lagrangian paths driven by a uniform Wiener process. As a stochastic representation of Kelvin's theorem, they proved that the circulation of the stochastic velocity defined for all realizations of the Wiener process is conserved. Similarly, Eyink (2009) extended the stochastic Lagrangian representation to resistive MHD flows by introducing a 'perturbed' velocity with a Brownian motion, and then Eyink *et al.* (2013) applied this formulation to analysing high-conductivity MHD turbulence. Gibbon & Holm (2010) derived a 'transport' velocity to investigate the frozen-in property of a flux vector related to the gradient of potential vorticity in oceans and atmosphere. Zhu, Yang & Zhu (2014) speculated that there might exist a 'fictitious' velocity for Garlerkin-truncated Euler's equation in which the helicity is conserved but the topology of vorticity is not conserved (see Moffatt 2014), so that Helmholtz's theorem can be extended to the truncated flows. Then Zhu (2018*a*,*b*) generalized the Lagrangian conservation laws and offered an alternative view based on the possible virtual velocity in the Lie-varying form for both HD and MHD flows.

These proposals of the virtual velocity provide a conceptual approach to understand vortex dynamics in non-ideal flows from a Lagrangian view, but they are restricted in local or stochastic formulations. The existence and uniqueness of a globally smooth virtual velocity remain an open problem in general three-dimensional non-ideal flows, so there is a lack of concrete, intuitive examples of the evolution of globally smooth vortex surfaces frozen in the virtual velocity in non-ideal flows. Moffatt (1978) pointed out that the concept of the virtual velocity, though physically appealing, can be misleading for complicated field structures. In general, the topology of a vorticity or magnetic field changes in non-ideal flows (see Kida & Takaoka 1994; Priest & Forbes 2000), which is in contradiction with the possible existence of a globally smooth virtual velocity. In the present study, we will elaborate the existence of the globally smooth virtual velocity and demonstrate that the formulation of the virtual velocity is useful for improving the understanding of vortex dynamics and the quantification of global vortex geometry and topology.

In order to characterize the evolution of global vortex surfaces, a couple of methods have been developed based on Lagrangian-like formulations and vorticity conservation

laws, and these methods could be improved with the virtual velocity. Clebsch (1859) proposed a Lagrangian formulation of ideal flow. In the Clebsch representation, the velocity is locally expressed in terms of three potential functions and each potential evolves as a Lagrangian scalar. The Clebsch representation was extended to build Eulerian–Lagrangian frameworks for NS dynamics (e.g. Constantin 2001; Ohkitani & Constantin 2003), but the construction of globally smooth Clebsch potentials except for a finite number of singularities is only successful in very few highly symmetric flows (He & Yang 2016).

Yang & Pullin (2010) proposed a framework of the vortex-surface field (VSF). The VSF is a globally smooth scalar field whose isosurface is a vortex surface consisting of vortex lines. The construction criterion for the VSF is weaker than that for Clebsch potentials, so we can construct approximate VSFs with very small deviations in a general three-dimensional flow field (see Xiong & Yang 2017). Furthermore, Yang & Pullin (2011) developed the two-time method with a dissipative numerical regularization to calculate and display the evolution of VSFs in real flows. The evolving VSF, as a Lagrangian-based structure identification method and a flow diagnostic tool, has been applied to transitional wall-bounded flows (Zhao, Yang & Chen 2016; Zhao *et al.* 2018), compressible flows (Peng & Yang 2018) and premixed combustion (Zhou *et al.* 2018). On the other hand, the numerical regularization still has uniqueness issues of VSF solutions, and the VSF has not been utilized in flows with strong non-ideal forces.

From the Lagrangian view, the vortex methods based on vortical elements such as vortex particles (see Cottet & Koumoutsakos 2000), vortex filaments (see Chorin 1994), and vortex sheets (e.g. Chorin & Bernard 1973; Lindsay & Krasny 2001) were developed to compute vortical flows by tracking a number of vortical elements. These methods require re-meshing and regularization techniques to deal with possible topological changes of the vortical elements.

When the Lagrangian-based methods are applied to non-ideal flows, the general issue is how to regularize the non-ideal effects on the motion of vortical structures. A deep understanding of the virtual velocity can be useful to elucidate the numerical regularization and improve the structure visualization and structure-based analysis.

In the present study, we will incorporate the virtual velocity into the existing VSF framework to track vortex surfaces in non-ideal flows. First, we will formally state several virtual conservation theorems of vorticity and related quantities in non-ideal flows with a smooth virtual velocity. Here, we add a prefix 'virtual' before the originally Lagrangian terms or theorems based on the physical velocity to represent the modified terms or theorems based on the virtual velocity, e.g. virtual material derivative and virtual Helmholtz's theorem. Second, we will provide the conditions for existence and uniqueness of a globally smooth virtual velocity, and some concrete examples to illustrate the physical meaning of the virtual velocity. Finally, we will demonstrate that the VSF with the virtual velocity can improve the flux conservation and time coherence of vortex tracking in flows with strong non-ideal forces and re-interpret vortex dynamics in the virtual Lagrangian view.

We remark that the vortical structures based on vorticity, such as vortex lines and surfaces (sometimes referred to as 'vorticity lines and surface' in the literature), have clear mathematical definitions. On the other hand, there is no consensus on the strict and unambiguous definition of a 'vortex' (see Haller 2005). Furthermore, most of the existing vortex identification criteria (e.g. Hunt, Wray & Moin 1988; Chong, Perry & Cantwell 1990; Jeong & Hussain 1995) based on the local velocity gradient tensor (see Gibbon, Galanti & Kerr 2000) are not related to the vorticity conservation laws

(see Wu 2018). Therefore, in the present study, we only focus on the tracking of vortex surfaces and the extension of vorticity conservation laws in non-ideal flows.

The outline of this paper is as follows. In § 2, we introduce the virtual velocity and virtual vorticity-related conservation theorems, and then discuss the existence and uniqueness of the virtual velocity. In § 3, we reformulate the existing VSF framework in terms of the virtual velocity. In § 4, we provide an overview of the numerical methods and set-up in the direct numerical simulation (DNS) of three-dimensional HD and MHD Taylor–Green (TG) flows and in the calculation of VSFs. Then we present and analyse the evolution of VSFs in HD and MHD TG flows in §§ 5 and 6, respectively. Some conclusions are drawn in § 7.

2. Virtual circulation-preserving velocity

2.1. *Introduction of the virtual velocity*

In a three-dimensional fluid flow, the Eulerian velocity $\boldsymbol{u} = (u_x, u_y, u_z)$ is governed by the NS equations, including the continuum equation

$$\frac{\partial \rho}{\partial t} + \boldsymbol{\nabla} \cdot (\rho \boldsymbol{u}) = 0, \tag{2.1}$$

the momentum equation

$$\frac{\partial \boldsymbol{u}}{\partial t} + (\boldsymbol{u} \cdot \boldsymbol{\nabla})\boldsymbol{u} = \boldsymbol{\nabla} \Pi + \boldsymbol{F}, \tag{2.2}$$

the energy equation and the equation of state. Here, $\Pi = -p/\rho + \Xi$ denotes a generalized potential with the pressure p, the density ρ and the potential Ξ of conservative body forces, and

$$\boldsymbol{F} = \frac{1}{\rho}(\boldsymbol{\nabla} \cdot \boldsymbol{\tau}) + p\boldsymbol{\nabla}\left(\frac{1}{\rho}\right) + \boldsymbol{f} \tag{2.3}$$

denotes a generalized non-ideal force term, where $\boldsymbol{\tau}$ is the viscous stress tensor and $\boldsymbol{f}$ is the non-conservative external body force per unit mass.

In a non-ideal flow, the three terms on the right-hand side of (2.3) respectively denote the viscous term in most real flows, the baroclinic term, e.g. in compressible flows and combustion, and the non-conservative body force term, e.g. the Lorentz force in MHD flows.

Taking curl of (2.2) yields the transport equation

$$\frac{\partial \boldsymbol{\omega}}{\partial t} - \boldsymbol{\nabla} \times (\boldsymbol{u} \times \boldsymbol{\omega}) = \boldsymbol{\nabla} \times \boldsymbol{F} \tag{2.4}$$

for the vorticity $\boldsymbol{\omega} \equiv \boldsymbol{\nabla} \times \boldsymbol{u}$. Helmholtz's vorticity theorem illustrates a frozen-in nature of $\boldsymbol{\omega}$ in ideal flows with $\boldsymbol{F} = 0$, whereas it breaks down in non-ideal flows, or, more precisely, in non-circulation-preserving flows with $\boldsymbol{\nabla} \times \boldsymbol{F} \neq 0$ (see Truesdell 1954). We remark that only a few non-ideal flows with trivial vortex dynamics are circulation-preserving, e.g. steady plane Couette and Poiseuille flows, so we do not strictly distinguish non-ideal and non-circulation-preserving flows in the present study.

Equivalently, Kelvin's circulation theorem is not valid for non-ideal flows with $\boldsymbol{\nabla} \times \boldsymbol{F} \neq 0$, i.e. the material derivative

$$\frac{\mathrm{D}}{\mathrm{D}t} \equiv \frac{\partial}{\partial t} + \boldsymbol{u} \cdot \boldsymbol{\nabla} \tag{2.5}$$

of the circulation $\Gamma \equiv \oint_{\mathcal{C}} \boldsymbol{u} \cdot \mathrm{d}\boldsymbol{l}$ round any closed material curve $\mathcal{C}$ that bounds an open material surface $\mathcal{S}$ has

$$\frac{\mathrm{D}\Gamma}{\mathrm{D}t} = \int_{\mathcal{S}} (\boldsymbol{\nabla} \times \boldsymbol{F}) \cdot \boldsymbol{n} \, \mathrm{d}\mathcal{S} \neq 0, \tag{2.6}$$

where $\mathrm{d}\boldsymbol{l}$ denotes a line element and $\boldsymbol{n}$ the normal of $\mathcal{S}$.

In order to extend Kelvin's theorem to non-ideal flows, we assume that there exists a smooth virtual velocity $\boldsymbol{v}$ determined by

$$\boldsymbol{\nabla} \times (\boldsymbol{v} \times \boldsymbol{\omega}) = \boldsymbol{\nabla} \times (\boldsymbol{u} \times \boldsymbol{\omega} + \boldsymbol{F}) \tag{2.7}$$

so that $\boldsymbol{\omega}$ is transported in $\boldsymbol{v}$ as

$$\frac{\partial \boldsymbol{\omega}}{\partial t} - \boldsymbol{\nabla} \times (\boldsymbol{v} \times \boldsymbol{\omega}) = 0. \tag{2.8}$$

This type of the virtual velocity was first introduced by Newcomb (1958) for the frozen-in motion of magnetic field lines in conducting flows, and it was revisited in the context of both HD and MHD flows (e.g. Greene 1993; Hornig & Schindler 1996; Zhu 2017).

2.2. *Virtual conservation theorems*

Based on the virtual velocity, Kelvin's theorem for ideal flows can be extended to non-ideal flows. Specifically, the virtual material derivative

$$\frac{\mathrm{D}_v}{\mathrm{D}_v t} \equiv \frac{\partial}{\partial t} + \boldsymbol{v} \cdot \boldsymbol{\nabla} \tag{2.9}$$

of Γ vanishes, where Γ is driven by the virtual velocity. This conservation law will be referred to as virtual Kelvin's theorem (see its proof in supplementary material available at https://doi.org/10.1017/jfm.2018.1014).

THEOREM 1 (virtual Kelvin's theorem). *Let $\mathcal{C}(t)$ be a closed curve moving with a globally smooth virtual velocity $\boldsymbol{v}$. Then the circulation Γ is a virtual Lagrangian scalar as*

$$\frac{\mathrm{D}_v \Gamma}{\mathrm{D}_v t} = 0. \tag{2.10}$$

Therefore, the flow of the virtual carrier velocity is circulation-preserving, and it is a special class of flows of significant interest (see Truesdell 1954; Wu, Ma & Zhou 2006). Then it is straightforward to extend the classical conservation theorems for vorticity kinematics in ideal flows to non-ideal flows with a smooth, circulation-preserving virtual velocity. The modified theorems below are referred to as virtual Helmholtz's theorem, virtual Ertel's theorem and the virtual conservation of helicity (see their proofs in the supplementary material). Similar extensions were discussed in different contexts for HD and MHD flows (see Greene 1993; Hornig & Schindler 1996; Wu *et al.* 2006). Additionally, more vorticity-based conservation laws (e.g. Cheviakov & Oberlack 2014) may be able to be extended to non-ideal flows.

THEOREM 2 (virtual Helmholtz's theorem). (1) *Let a vortex tube move with a globally smooth virtual velocity, and then the vorticity flux*

$$\Phi = \int_{\mathcal{S}} \boldsymbol{\omega} \cdot \boldsymbol{n} \, \mathrm{d}\mathcal{S} \tag{2.11}$$

through cross-section $\mathcal{S}$ of the vortex tube is a virtual Lagrangian scalar as

$$\frac{\mathrm{D}_v \Phi}{\mathrm{D}_v t} = 0. \tag{2.12}$$

(2) *Let a vortex line move with a globally smooth virtual velocity, and then the line elements moving with the virtual velocity lying on the vortex line at some instant continue to lie on that vortex line, i.e.*

$$\frac{\mathrm{D}_v}{\mathrm{D}_v t}\left(\frac{\boldsymbol{\omega}}{\rho} \times \delta \boldsymbol{l}\right) = 0 \tag{2.13}$$

is satisfied with the initial condition

$$\frac{\boldsymbol{\omega}}{\rho} \times \delta \boldsymbol{l} = 0. \tag{2.14}$$

Strictly speaking, the requirement of $\boldsymbol{v}$ for flux-conservation in (1) of virtual Helmholtz's theorem is stronger than that for line-preserving in (2). In other words, for only satisfying the virtual line-preserving in (2), the constraint (2.7) of $\boldsymbol{v}$ can be relaxed to

$$\nabla \times (\boldsymbol{v} \times \boldsymbol{\omega}) = \nabla \times (\boldsymbol{u} \times \boldsymbol{\omega} + \boldsymbol{F}) - \lambda \boldsymbol{\omega}, \tag{2.15}$$

with an arbitrary scalar λ (see Truesdell 1954).

THEOREM 3 (virtual Ertel's theorem). *Let ϕ be a virtual Lagrangian scalar convected by a globally smooth virtual velocity as*

$$\frac{\mathrm{D}_v \phi}{\mathrm{D}_v t} = 0, \tag{2.16}$$

with

$$\frac{\boldsymbol{\omega}}{\rho} \cdot \nabla \phi = 0 \tag{2.17}$$

at the initial time, and then $(\boldsymbol{\omega}/\rho) \cdot \nabla \phi$ is also a virtual Lagrangian scalar as

$$\frac{\mathrm{D}_v}{\mathrm{D}_v t}\left(\frac{\boldsymbol{\omega}}{\rho} \cdot \nabla \phi\right) = 0. \tag{2.18}$$

THEOREM 4 (virtual conservation of helicity). *Let a volume $\mathcal{V}(t)$ enclosed by a vortex surface move with a globally smooth virtual velocity, and then the helicity is a virtual Lagrangian scalar as*

$$\frac{\mathrm{D}_v H}{\mathrm{D}_v t} = 0. \tag{2.19}$$

Here, the helicity (Moreau 1961; Moffatt 1969)

$$H \equiv \int_{\mathcal{V}} \boldsymbol{\omega} \cdot \boldsymbol{u} \, \mathrm{d}\mathcal{V} \tag{2.20}$$

characterizes the topology of vortex lines in the volume $\mathcal{V}$ enclosed by a vortex surface.

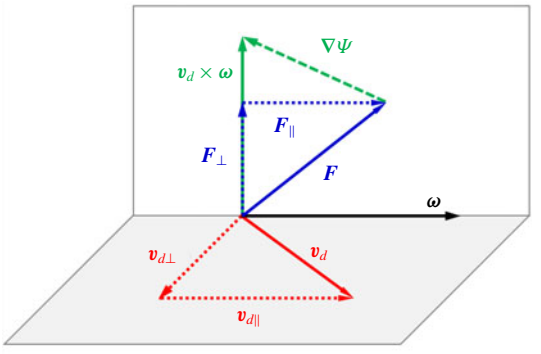

FIGURE 1. (Colour online) Diagram of the vorticity-based orthogonal decompositions of the non-ideal force and the virtual velocity.

2.3. *Determination of the virtual velocity*

Although the form of (2.8) is very appealing for vorticity dynamics due to the virtual frozen-in nature of $\boldsymbol{\omega}$, the determination of globally smooth $\boldsymbol{v}$ can be challenging. First we re-express (2.7) as

$$\boldsymbol{v}_d \times \boldsymbol{\omega} = \boldsymbol{F} + \nabla\Psi, \tag{2.21}$$

where $\boldsymbol{v}_d \equiv \boldsymbol{v} - \boldsymbol{u}$ denotes a drift velocity and Ψ is an arbitrary gauge. As sketched in figure 1, we introduce a vorticity-based orthogonal decomposition

$$\boldsymbol{v}_d = \boldsymbol{v}_{d\perp} + \boldsymbol{v}_{d\parallel}, \tag{2.22}$$

where $\boldsymbol{v}_{d\perp}$ and $\boldsymbol{v}_{d\parallel}$ are respectively perpendicular and parallel to $\boldsymbol{\omega}$, and we can only determine $\boldsymbol{v}_{d\perp}$ from (2.21). The parallel component

$$\boldsymbol{v}_{d\parallel} = C_\parallel \boldsymbol{\omega} \tag{2.23}$$

with a constant or scalar function $C_\parallel$ can be arbitrary owing to $\boldsymbol{v}_{d\parallel} \times \boldsymbol{\omega} = 0$ in (2.7).

By taking the cross-product of $\boldsymbol{\omega}$ with (2.21), we obtain

$$\boldsymbol{v}_{d\perp} = \frac{\boldsymbol{\omega} \times (\boldsymbol{F} + \nabla\Psi)}{\omega^2}, \tag{2.24}$$

where $\omega \equiv |\boldsymbol{\omega}|$ is the magnitude of vorticity, and by taking the inner product of $\boldsymbol{\omega}$ with (2.21), Ψ in (2.24) satisfies

$$\boldsymbol{F} \cdot \boldsymbol{\omega} = -\boldsymbol{\omega} \cdot \nabla\Psi. \tag{2.25}$$

From (2.22) and (2.24), the virtual velocity is

$$\boldsymbol{v} = \boldsymbol{u} + \frac{\boldsymbol{\omega} \times (\boldsymbol{F} + \nabla\Psi)}{\omega^2} + C_\parallel \boldsymbol{\omega}, \tag{2.26}$$

which is in general not divergence-free. Appendix A.1 provides an example of the virtual velocity and illustrates its physical meaning in a two-dimensional TG flow.

It is noted that (2.25) can be satisfied locally (Greene 1993), but a necessary condition for the existence and uniqueness of globally smooth solutions to the first-order partial differential equation of the type (2.25) with various boundary conditions is generally not clear. For example, the analysis of Huang, Küpper & Masbaum (1997) showed that the existence and uniqueness of solutions to (2.25) with periodic conditions are not satisfied.

2.4. *Existence and uniqueness of the virtual velocity*

Since the existence and uniqueness of an explicit and globally smooth solution of $\boldsymbol{v}$ are not ensured in general non-ideal flows, we have to seek explicit $\boldsymbol{v}$ in the flows with special non-ideal forces. As sketched in figure 1, we apply the vorticity-based orthogonal decomposition to the non-ideal force in (2.2) as

$$\boldsymbol{F} = \boldsymbol{F}_\perp + \boldsymbol{F}_\parallel, \tag{2.27}$$

where

$$\boldsymbol{F}_\perp = \boldsymbol{F} - \frac{\boldsymbol{F}\cdot\boldsymbol{\omega}}{\omega^2}\boldsymbol{\omega} \tag{2.28}$$

is the component of $\boldsymbol{F}$ perpendicular to $\boldsymbol{\omega}$ and $\boldsymbol{F}_\parallel$ is the vorticity-parallel component. We remark that the decomposition is meaningless and the virtual velocity becomes singular at the points with $\omega = 0$, i.e. vorticity nulls or 'vortex nulls' (Saffman 1992).

Owing to the difficulty of determining Ψ from (2.25), we suppose that, in some particular cases, $\boldsymbol{F}_\parallel$ is irrotational or there exists a globally smooth Ψ satisfying

$$\boldsymbol{F}_\parallel = -\nabla\Psi. \tag{2.29}$$

As illustrated in figure 1, this choice has minimum $|\nabla\Psi|$ in all the possible $\nabla\Psi$. Thus from (2.24) we can exactly determine

$$\boldsymbol{v}_{d\perp} = \frac{\boldsymbol{\omega}\times\boldsymbol{F}_\perp}{\omega^2}. \tag{2.30}$$

A special case of (2.29) is $\boldsymbol{F}_\parallel = 0$, and (2.25) becomes

$$\boldsymbol{F}\cdot\boldsymbol{\omega} = 0. \tag{2.31}$$

We remark that

$$\nabla\times\boldsymbol{F}_\parallel = 0 \tag{2.32}$$

is a sufficient condition for the existence of non-trivial smooth $\boldsymbol{v}$ at the points with $\omega \neq 0$. Appendix A.2 provides an example of an exact solution of $\boldsymbol{v}$ with $\nabla\times\boldsymbol{F}_\parallel \neq 0$ in an integrable Arnold–Beltrami–Childress (ABC) flow.

Remark 1. The sufficient conditions for applying Theorems 1–4 for the virtual conservation of a vorticity-related structure (e.g. a loop, vortex line, vortex surface or VSF) moving with a globally smooth virtual velocity are specified as follows. In a finite region where the vorticity-related structure sweeps,

(i) the local non-ideal force has $\nabla\times\boldsymbol{F}_\parallel = 0$; and
(ii) the local vorticity does not vanish.

If there exist globally smooth solutions of $\boldsymbol{v}_d$, we need additional constraints to determine a unique virtual velocity. First, the choice of $\boldsymbol{v}_\parallel$ in (2.26) does not affect vorticity transport in (2.8), so we can choose $C_\parallel = 0$ in (2.26) without loss of generality. Second, if the solution of Ψ for (2.25) exists but is not unique, we propose an additional constraint

$$\min\langle|\nabla\Psi|\rangle \tag{2.33}$$

to determine unique $\nabla\Psi$, where $\langle\cdot\rangle$ denotes the volume average. This constraint makes the virtual velocity finite and smooth, and it is consistent with (2.29) under condition (2.32). Taking a two-dimensional flow for example, we obtain $\boldsymbol{v}_d = -\nu\nabla\omega/\omega$ from (2.30) with $\boldsymbol{F}_\parallel = 0$. Moreover, it is possible to calculate an approximate virtual velocity using numerical methods, which is out of scope of the present study.

2.5. *Virtual velocity in modified fluid flows*

Given the difficulty for determining a globally smooth virtual velocity in real flows, we propose a modified fluid flow in which explicit $\boldsymbol{v}$ can be obtained. This modified flow is artificial and only used for the theoretical study of accurately tracking vortex surfaces.

For simplicity, we consider an incompressible barotropic viscous flow governed by

$$\left.\begin{gathered}\frac{\partial \boldsymbol{u}}{\partial t}+\boldsymbol{u}\cdot\nabla\boldsymbol{u}=-\frac{1}{\rho}\nabla p+\boldsymbol{F},\\ \nabla\cdot\boldsymbol{u}=0.\end{gathered}\right\} \tag{2.34}$$

The requirement (2.32) can be satisfied by imposing $\boldsymbol{F}_{\parallel}=0$. Thus we obtain a modified NS (MNS) equation:

$$\frac{\partial \boldsymbol{u}}{\partial t}+\boldsymbol{u}\cdot\nabla\boldsymbol{u}=-\frac{1}{\rho}\nabla p+\boldsymbol{F}_{\perp}. \tag{2.35}$$

This equation can be valid in some real flows, e.g. two-dimensional flows, or in a modified flow with a special constitutive relation. Then the vorticity equation becomes

$$\frac{\partial \boldsymbol{\omega}}{\partial t}=\nabla\times(\boldsymbol{u}\times\boldsymbol{\omega})+\nabla\times\boldsymbol{F}_{\perp}. \tag{2.36}$$

For the MNS equation, we set $\Psi=0$ based on (2.33) and $C_{\parallel}=0$ in (2.23), then we uniquely determine the virtual velocity (2.26) as

$$\boldsymbol{v}=\boldsymbol{u}+\frac{\boldsymbol{\omega}\times\boldsymbol{F}_{\perp}}{\omega^2}. \tag{2.37}$$

The modified flow governed by (2.35) has virtual Kelvin's theorem and other virtual vorticity conservation theorems in § 2.2 except at vorticity nulls. Thus the virtual evolution of vortex lines or surfaces can be topologically invariant in the modified dissipative flow. Here, we only consider a modified viscous term in $\boldsymbol{F}_{\perp}$ as

$$\boldsymbol{F}_{\perp}=\nu\left[\nabla^2\boldsymbol{u}-\frac{(\nabla^2\boldsymbol{u}\cdot\boldsymbol{\omega})\boldsymbol{\omega}}{\omega^2}\right]. \tag{2.38}$$

The corresponding drift velocity (2.37) becomes

$$\boldsymbol{v}_d=\nu\frac{(\nabla\times\boldsymbol{\omega})\times\boldsymbol{\omega}}{\omega^2}=-\nu\frac{\nabla\omega}{\omega}+\nu\frac{(\boldsymbol{\omega}\cdot\nabla)\boldsymbol{\omega}}{\omega^2}, \tag{2.39}$$

where the first term on the right-hand side denotes a velocity pointing from high-ω region to low-ω region, and the second term appears to be highly nonlinear in three-dimensional flows and it vanishes in two-dimensional flows.

The transport equation for the enstrophy $\Omega\equiv\omega^2/2$ in the modified fluid is derived from (2.36) as

$$\frac{\mathrm{D}\Omega}{\mathrm{D}t}=\boldsymbol{\omega}\cdot\boldsymbol{S}\cdot\boldsymbol{\omega}+\boldsymbol{\omega}\cdot(\nabla\times\boldsymbol{F}_{\perp}), \tag{2.40}$$

where $\boldsymbol{S}\equiv(\nabla\boldsymbol{u}+\nabla\boldsymbol{u}^T)/2$ is the rate-of-strain tensor. Substituting (2.38) into (2.40) yields

$$\frac{\mathrm{D}\Omega}{\mathrm{D}t}=\boldsymbol{\omega}\cdot\boldsymbol{S}\cdot\boldsymbol{\omega}+\nu\{-(\sin^2\vartheta_{\omega})(\nabla^2\boldsymbol{u})^2+\nabla\cdot[\boldsymbol{\omega}\times(\nabla\times\boldsymbol{\omega})]\} \tag{2.41}$$

after some algebra, where ϑ_ω denotes the angle between $\boldsymbol{\omega}$ and $\nabla^2\boldsymbol{u}$. Comparing (2.41) and the enstrophy equation (see Davidson 2004)

$$\frac{\mathrm{D}\Omega}{\mathrm{D}t} = \boldsymbol{\omega}\cdot\boldsymbol{S}\cdot\boldsymbol{\omega} + \nu\{-(\nabla^2\boldsymbol{u})^2 + \nabla\cdot[\boldsymbol{\omega}\times(\nabla\times\boldsymbol{\omega})]\} \tag{2.42}$$

for real fluid flows with the NS equation (2.2), we find that the prefactor $0 \leqslant \sin^2\vartheta_\omega \leqslant 1$ of the second term on the right-hand side of (2.41) weakens the enstrophy dissipation term in the modified fluid flow without the vorticity-parallel component of the viscous term in the MNS equation (2.35). Thus this modified fluid flow is dissipative, but less dissipative than real flows.

As another example of the modified fluid, in the framework of incompressible Schrödinger flow (ISF) (Chern *et al.* 2016), the ideal flow is modified by a 'Landau–Lifshitz term' which shares some physical features in superfluids. As discussed in § A.3, we find that this non-ideal term is also orthogonal to the vorticity, so it can be included in the drift velocity. Chern (2017) argued that the drift velocity (also referred to as 'Landau–Lifshitz velocity' in ISF) regularizes the Euler equation and enhances additional localized induction of vortex filaments.

3. Reformulation of the VSF with the virtual velocity

3.1. *Original formulation of the VSF*

The VSF is a Lagrangian-based structure identification method rooted in Helmholtz's theorem. The VSF is defined as a smooth scalar field satisfying the constraint (see Yang & Pullin 2010)

$$\boldsymbol{\omega}\cdot\nabla\phi_v = 0, \tag{3.1}$$

so that $\boldsymbol{\omega}$ is tangent at every point on an isosurface of ϕ_v. Namely, each VSF isosurface is a vortex surface consisting of vortex lines.

In order to characterize the temporal evolution of VSFs, we seek $\phi_v(\boldsymbol{x}, t)$ satisfying constraint (3.1) at all time as

$$\frac{\mathrm{D}}{\mathrm{D}t}(\boldsymbol{\omega}\cdot\nabla\phi_v) = 0. \tag{3.2}$$

Similar to the derivation in Yang & Pullin (2010), we derive the evolution equation for the VSF from (2.4) and (3.2) as

$$\frac{\mathrm{D}\phi_v}{\mathrm{D}t} = \mathscr{L}, \tag{3.3}$$

with

$$\nabla\phi_v\cdot(\nabla\times\boldsymbol{F}) + \boldsymbol{\omega}\cdot\nabla\mathscr{L} - (\nabla\cdot\boldsymbol{v})\boldsymbol{\omega}\cdot\nabla\phi_v = 0, \tag{3.4}$$

where $\mathscr{L}$ is a scalar field and represents the effects of non-ideal forces on the evolution of VSF.

Similar to the difficulty of (2.25) in determining the virtual velocity, the existence and uniqueness of solutions to the first-order partial differential equation (3.4) for $\mathscr{L}$ are also an open problem. A two-time method is developed to numerically solve (3.3) and (3.4) by introducing a dissipative numerical regularization (Yang & Pullin 2011). Although the numerical method has been successfully applied to highly symmetric flows and transitional channel flows (Zhao *et al.* 2016), the numerical regularization still has the uniqueness issue of VSF solutions.

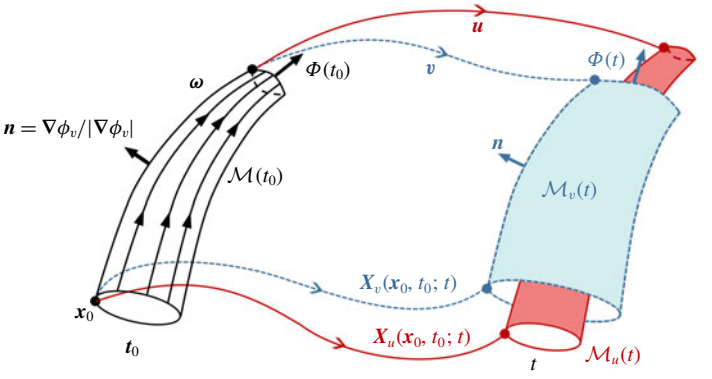

FIGURE 2. (Colour online) Sketch of the surface evolution convected by the virtual or physical velocity in a non-ideal flow. At time t_0, the black solid surface denotes the initial vortex tube $\mathcal{M}(t_0)$ with vortex lines (black lines with arrows), the surface normal $\boldsymbol{n} = \nabla\phi_v/|\nabla\phi_v|$ and the vorticity flux $\Phi(t_0)$. At time t, the blue surface $\mathcal{M}_v(t_0)$ denotes the vortex surface convected by $\boldsymbol{v}$; the red surface $\mathcal{M}_u(t_0)$ denotes the material surface convected by $\boldsymbol{u}$. The dotted blue and solid red lines with arrows denote trajectories of $\boldsymbol{X}_v(\boldsymbol{x}_0, t_0; t)$ and $\boldsymbol{X}_u(\boldsymbol{x}_0, t_0; t)$ from the same initial position $\boldsymbol{x}_0$ but convected by $\boldsymbol{v}$ and $\boldsymbol{u}$, respectively.

3.2. *Transport of the VSF in the virtual velocity*

Based on the virtual velocity, we reformulate transport equations of the VSF in non-ideal flows. If ϕ_v is a VSF at an initial time and it evolves as $\mathrm{D}\phi_v/\mathrm{D}t = 0$, it is always a VSF satisfying (3.2) at all time in ideal flows from Ertel's theorem. Although this frozen-in nature of VSF breaks down in non-ideal flows, the form of (3.2) can be still valid in the virtual velocity.

Considering ϕ_v is convected along a globally smooth virtual velocity as

$$\frac{\mathrm{D}_v\phi_v}{\mathrm{D}_v t} = 0, \tag{3.5}$$

with a VSF initial condition, from (2.18) in virtual Ertel's theorem without considering ρ, we have

$$\frac{\mathrm{D}_v}{\mathrm{D}_v t}(\boldsymbol{\omega}\cdot\nabla\phi_v) = 0. \tag{3.6}$$

Thus we can exactly track the VSF from (3.5) from the virtual Lagrangian view.

The tracking of a vortex surface (or tube) frozen in the virtual velocity in a non-ideal flow is sketched in figure 2, and the tracking of a material surface from the same initial surface is also shown for comparison. From the Lagrangian view, the surface tracking in the narrow sense is described by the flow map of a surface. Evolving from the same vortex surface $\mathcal{M}(t_0)$ at initial time t_0,

$$\mathcal{M}_v(t) := \mathcal{F}^t_{t_0,v}(\mathcal{M}(t_0)) \quad \text{and} \quad \mathcal{M}_u(t) := \mathcal{F}^t_{t_0,u}(\mathcal{M}(t_0)) \tag{3.7a,b}$$

denote the vortex surface convected by $\boldsymbol{v}$ and the material surface convected by $\boldsymbol{u}$, respectively, where the flow maps are defined as

$$\mathcal{F}^t_{t_0,v}(\boldsymbol{x}_0) := \boldsymbol{X}_v(\boldsymbol{x}_0, t_0; t) \quad \text{and} \quad \mathcal{F}^t_{t_0,u}(\boldsymbol{x}_0) := \boldsymbol{X}_u(\boldsymbol{x}_0, t_0; t). \tag{3.8a,b}$$

Here, the Lagrangian coordinates $\boldsymbol{X}_v(\boldsymbol{x}_0,\ t_0;\ t)$ convected by $\boldsymbol{v}$ and $\boldsymbol{X}_u(\boldsymbol{x}_0,\ t_0;\ t)$ convected by $\boldsymbol{u}$ are governed by

$$\frac{\mathrm{D}\boldsymbol{X}_v}{\mathrm{D}t} = \boldsymbol{v}(\boldsymbol{X}_v, t) \quad \text{and} \quad \frac{\mathrm{D}\boldsymbol{X}_u}{\mathrm{D}t} = \boldsymbol{u}(\boldsymbol{X}_u, t), \tag{3.9a,b}$$

respectively, and the coordinates are labelled at the same initial position $\boldsymbol{x}_0$.

In terms of the VSF, the vortex surface is an isosurface of ϕ_v at a particular isocontour value, where ϕ_v is governed by (3.5). The vorticity flux $\Phi(t)$ through a cross-section of vortex tube $\mathcal{M}_v(t)$ is conserved from (2.12) in virtual Helmholtz's theorem. The surfaces $\mathcal{M}_v(t)$ and $\mathcal{M}_u(t)$ are the same in ideal flows, whereas they are different in non-ideal flows. As discussed in § A.1 and illustrated in figure 2, the viscous effect can diminish the vorticity flux, so the radius of the vortex tube $\mathcal{M}_v(t)$ can be larger than that of the material one $\mathcal{M}_v(t)$ to keep vorticity flux $\Phi(t) = \Phi(t_0)$ invariant.

Furthermore, the helicity is conserved in ideal flows, but not conserved in non-ideal flows, i.e. vortex lines or surfaces can have reconnection. From (2.19) in the virtual helicity conservation theorem, the helicity is still conserved in a virtual material volume convected along the virtual velocity. This implies that topological properties of vortex lines within a virtual material volume are invariant, and this topological invariance breaks down at vorticity nulls owing to the singular virtual velocity.

Although both VSF formulations (3.3) and (3.5) have the common difficulty on solving first-order partial differential equations, the VSF formulation with the virtual velocity provides a physical explanation of the VSF transport in non-ideal flows. If a globally smooth virtual velocity exists, the VSF isosurface is the carrier for Theorems 2–4, which will be discussed in § 5. If not, an approximate virtual velocity can be still useful to reduce the deviation from the virtual conservation theorems in VSF calculation, which will be discussed in § 6.

4. Simulation overview

4.1. *DNS of HD TG flows*

The DNS of HD flows is used to solve the incompressible NS equation (2.34) with $\boldsymbol{F} = \nu\nabla^2\boldsymbol{u}$ and the MNS equation (2.35) with $\boldsymbol{F}_\perp$ (2.38) in a periodic cube of side 2π. The HD TG flow evolution from the TG initial condition (Taylor & Green 1937)

$$\boldsymbol{u}_0 = (\sin x \cos y \cos z,\ -\cos x \sin y \cos z,\ 0) \tag{4.1}$$

has a transitional process with the rapid development of small-scale vortical structures as energy cascade. Within the periodic cube, there are multiple mirror symmetries, anti-symmetries and rotational symmetries with fixed vorticity nulls at the intersections of symmetric planes (see Brachet *et al.* 1983). These symmetries were utilized to reduce the computational cost for calculating the evolution of VSFs.

The DNS was carried out using the standard pseudo-spectral method on uniform grid points $N^3 = 512^3$ at the Reynolds number $Re \equiv 1/\nu = 100$. The spatial resolution is high enough for the TG flow at such a low Re (Brachet *et al.* 1983). Aliasing errors were removed using the two-thirds dealiasing rule with the maximum wavenumber $k_{max} = N/3$. The temporal integration of the Fourier coefficients of $\boldsymbol{u}$ was performed using a second-order Runge–Kutta scheme. The time step Δt was selected to ensure that the Courant–Friedrichs–Lewy (CFL) number

$$\mathrm{CFL} = \frac{\Delta t}{\Delta x}\max(|u_x|, |u_y|, |u_z|) \tag{4.2}$$

is less than 0.5 for numerical stability and accuracy, where $\Delta x = 2\pi/N$ denotes the grid spacing. Moreover, the singular modified viscous term (2.38) at vorticity nulls was smoothed by multiplying a smoothing coefficient $C_\epsilon = \omega^2/(\omega^2 + \epsilon)$ in the MNS equation (2.35) with $\epsilon = 1 \times 10^{-6}$.

4.2. *DNS of MHD TG flows*

The incompressible MHD equations in terms of dimensionless velocity $\boldsymbol{u}$ and magnetic induction $\boldsymbol{b}$ read (e.g. see Priest & Forbes 2000)

$$\left.\begin{aligned} \frac{\partial \boldsymbol{u}}{\partial t} + \boldsymbol{u}\cdot\nabla\boldsymbol{u} &= -\frac{1}{\rho}\nabla p + \boldsymbol{j}\times\boldsymbol{b} + \nu\nabla^2\boldsymbol{u}, \\ \frac{\partial \boldsymbol{b}}{\partial t} &= \nabla\times(\boldsymbol{u}\times\boldsymbol{b}) + \eta\nabla^2\boldsymbol{b}, \end{aligned}\right\} \tag{4.3}$$

together with $\nabla\cdot\boldsymbol{u} = 0$ and $\nabla\cdot\boldsymbol{b} = 0$, where η denotes the magnetic diffusivity and $\boldsymbol{j} = \nabla\times\boldsymbol{b}$ the current density. We define the magnetic Reynolds number $Rm = 1/\eta$, and assume that the MHD flows in DNS have the unity magnetic Prandtl number with $Re = Rm$.

The same TG initial velocity (4.1) is applied in the DNS of MHD flows. Additionally, two TG-type initial magnetic fields are considered. The first one is the steady initial condition with $\boldsymbol{b}_0 = \boldsymbol{u}_0$. For this steady case, MHD equations (4.3) degenerate into pure diffusion equations

$$\frac{\partial \boldsymbol{\omega}}{\partial t} = \nu\nabla^2\boldsymbol{\omega} \quad \text{and} \quad \frac{\partial \boldsymbol{b}}{\partial t} = \eta\nabla^2\boldsymbol{b}. \tag{4.4a,b}$$

The second initial magnetic field is the 'insulating' condition (see Lee *et al.* 2009)

$$\boldsymbol{b}_0 = b_0(\cos x \sin y \sin z,\ \sin x \cos y \sin z,\ -2\sin x \sin y \cos z), \tag{4.5}$$

with $b_0 = 1/\sqrt{3}$. For this initial condition, the current $\boldsymbol{j}$ is contained within each 'insulating box', e.g. $[0, \pi]^3$, and $\boldsymbol{b}$ is proportional to $\boldsymbol{\omega}$ at the initial time.

As in the DNS of HD flows, the DNS of MHD flows was also carried out on uniform grid points $N^3 = 512^3$ in a periodic cube with side 2π. A symmetric form of (4.3) with the Elsässer variables $\boldsymbol{z}^\pm = \boldsymbol{u} \pm \boldsymbol{b}$ (see Elsässer 1950) is solved using the pseudo-spectral method (see Aluie 2009). The two-thirds dealiasing rule was applied and the temporal integration was performed using a second-order Runge–Kutta scheme.

4.3. *Calculation of VSFs*

First, initial VSF ϕ_{v0} is constructed to satisfy the VSF constraint (3.1). For the TG initial velocity (4.1), the initial VSF is

$$\phi_{v0} = (\cos 2x - \cos 2y)\cos z. \tag{4.6}$$

Then the evolution of the VSF is calculated using the two-time method (Yang & Pullin 2011). Each time step is divided into prediction and correction sub-steps. In the prediction sub-step, the temporary VSF ϕ_v^* is driven by an advection velocity $\boldsymbol{V}$ as

$$\frac{\partial \phi_v^*(\boldsymbol{x}, t)}{\partial t} + \boldsymbol{V}(\boldsymbol{x}, t)\cdot\nabla\phi_v^*(\boldsymbol{x}, t) = 0, \quad t > 0. \tag{4.7}$$

Case	Equation for $\boldsymbol{u}$	$\boldsymbol{V}$ in (4.7)
HD-NS	(2.2)	$\boldsymbol{u}$
HD-MNS	(2.35)	$\boldsymbol{u}+\nu(\boldsymbol{\omega}\times\nabla^2\boldsymbol{u})/\omega^2$
MHD-S	(4.3)	$\boldsymbol{u}$
MHD-SV	(4.3)	0
MHD-I	(4.3)	$\boldsymbol{u}$
MHD-IV	(4.3)	$\boldsymbol{u}+[\boldsymbol{\omega}\times(\boldsymbol{j}\times\boldsymbol{b})]/\omega^2$

TABLE 1. Set-up of different DNS cases and corresponding VSF calculations.

In the correction sub-step, ϕ_v^* is driven by the frozen vorticity at a fixed physical time t and evolved in pseudo time τ as

$$\frac{\partial\phi_v^*(\boldsymbol{x},t;\tau)}{\partial t}+\boldsymbol{\omega}(\boldsymbol{x},t)\cdot\nabla\phi_v^*(\boldsymbol{x},t;\tau)=0,\quad 0<\tau\leqslant T_\tau, \tag{4.8}$$

where the initial condition is $\phi_v(\boldsymbol{x},t;\tau=0)=\phi_v^*(\boldsymbol{x},t)$. At the end of the correction sub-step, ϕ_v is updated by $\phi_v^*(\boldsymbol{x},t;\tau=T_\tau)$, where T_τ is the maximum pseudo time and is typically less than 100 times Δt.

Different choices of $\boldsymbol{V}$ in (4.7), either the physical velocity for solving (3.3) or the virtual velocity for solving (3.5), are applied for different DNS cases, and they are summarized in table 1. If $\boldsymbol{V}$ is a physical velocity, the temporary ϕ_v^* deviates from an accurate VSF owing to the breakdown of Helmholtz's theorem in non-ideal flows. In the correction sub-step, the temporary ϕ_v^* in the VSF evolution is convected along the frozen vorticity in (4.8), which projects ϕ_v^* onto the desired VSF solution. If $\boldsymbol{V}$ is a virtual velocity, the correction sub-step only serves as a further numerical correction for preserving the isosurfaces of ϕ_v as vortex surfaces.

The numerical schemes for solving (4.7) and (4.8) are described in detail in Yang & Pullin (2011). Temporal integrations are marched by the third-order total-variation-diminishing Runge–Kutta scheme (see Gottlieb & Shu 1998). The time steps Δt and $\Delta\tau$ were chosen to ensure the corresponding CFL conditions based on $\boldsymbol{V}$ and $\boldsymbol{\omega}$, respectively. The convection terms were treated by the fifth-order weighted essentially non-oscillatory (WENO) scheme (see Jiang & Shu 1996) and the numerical diffusion in the WENO scheme serves as a numerical dissipative regularization for removing small-scale, nearly singular scalar structures. The computational domain for the VSF calculation was selected as $\boldsymbol{x}\in[0,\pi/2]\times[0,\pi/2]\times[\pi/2,\pi]$. The periodic condition and other boundary conditions under TG symmetries (see Yang & Pullin 2010) were applied. The grid resolution for the VSF in the periodic cube is $N^3=512^3$, the same as that for the velocity field in both HD and MHD flows. Additionally, the singular drift velocity at vorticity nulls in case MHD-IV was smoothed as $C_\epsilon\boldsymbol{v}_d$.

In practice, the computed ϕ_v can have a small deviation from an exact VSF owing to the numerical regularization. The VSF deviation (see Yang & Pullin 2010) is quantified by the cosine of the angle between the vorticity field $\boldsymbol{\omega}$ and the gradient of VSF $\nabla\phi_v$ as

$$\lambda_\omega=\frac{\boldsymbol{\omega}\cdot\nabla\phi_v}{|\boldsymbol{\omega}|\,|\nabla\phi_v|}. \tag{4.9}$$

Thus an exact VSF solution has $\lambda_\omega=0$, and a relatively accurate numerical solution should have a small enough $\langle|\lambda_\omega|\rangle$ so that we can extract isosurfaces of the VSF solution to study the evolution of vortex surfaces.

4.4. *Error estimation for the approximated virtual velocity used in VSF calculation*

Although conceptually the VSF can be tracked from the virtual Lagrangian view by setting the advection velocity as the virtual velocity in (3.5), the conditions for the existence and uniqueness of (2.30) are not ensured in general three-dimensional flows. For VSF calculation, if we use the explicit expression (2.37), which is only exact for the modified fluid flows with $\nabla \times \boldsymbol{F}_{\parallel} \neq 0$, to approximate the general virtual velocity (2.26) in (3.5), the deviation owing to the absence of $\nabla\Psi$ is defined as

$$\epsilon_{\Psi} \equiv \frac{(\boldsymbol{\omega} \times \nabla\Psi) \cdot \nabla\phi_v}{\omega^2}, \tag{4.10}$$

with constraint equations (2.25) and (3.1).

Next we provide an order analysis of ϵ_{Ψ} as an error estimation for the approximate virtual velocity (2.37) used in VSF calculation. Here, we assume $\boldsymbol{F}$ has a preferential normal alignment with $\boldsymbol{\omega}$ in a particular flow evolution, and then

$$\boldsymbol{\omega} \cdot \nabla\Psi = \delta_F \tag{4.11}$$

is very small from (2.25). This assumption implies that

$$|\nabla\Psi| = \frac{\delta_F}{\omega \cos\vartheta_F}, \tag{4.12}$$

where ϑ_F denotes the angle between $\boldsymbol{F}$ and $\boldsymbol{\omega}$. Substituting (4.12) into (4.10) yields

$$O(\epsilon_{\Psi}) \sim O\left(\frac{|\delta_F|\,|\nabla\phi_v|\,|\tan\vartheta_F|}{\omega^2}\right). \tag{4.13}$$

Considering the uniqueness constraint (2.33), which is equivalent to $\max\langle|\cos\vartheta_F|\rangle$ in (4.12) or $\min\langle|\tan\vartheta_F|\rangle$ in (4.13), (4.13) becomes $O(\epsilon_{\Psi}) \sim O(|\delta_F|\,|\nabla\phi_v|/\omega^2)$, and it can be small if we track the VSF frozen in (2.37) in the non-ideal flow with small $\boldsymbol{F}_{\parallel}$.

5. VSF evolution in HD TG flows

5.1. *Statistics in real and modified flows*

In order to investigate the influence of vorticity-parallel and vorticity-normal non-ideal force components on flow evolution, we carry out DNS cases HD-NS and HD-MNS (see table 1) at $Re = 100$. The temporal evolutions of the total kinetic energy $E_k \equiv \langle|\boldsymbol{u}|^2\rangle/2$ and enstrophy Ω in the two cases are compared in figure 3. We find that the decay of E_k in HD-MNS is slower than that in HD-NS, and $\langle\Omega\rangle$ in HD-MNS is always larger than that in HD-NS. This observation agrees with the theoretical analysis by comparing (2.41) and (2.42), i.e. the modified fluid flow is less dissipative than the real fluid flow.

The averaged VSF deviations in two VSF calculations with different $\boldsymbol{V}$ in (4.7) in HD-NS and HD-MNS (see table 1) are compared in figure 4. Both $\langle|\lambda_{\omega}|\rangle$ are very small (less than 1 %) at $t \leqslant 4$ in the temporal evolution of VSFs, and $\langle|\lambda_{\omega}|\rangle$ in HD-MNS is even less than 0.1 % and is much smaller than that in HD-NS. For comparison, if we evolve ϕ_v as a passive scalar as (4.7) driven by physical velocity $\boldsymbol{u}$ with the same initial VSF ϕ_{v0}, the VSF deviation at $t = 4$ is relatively large

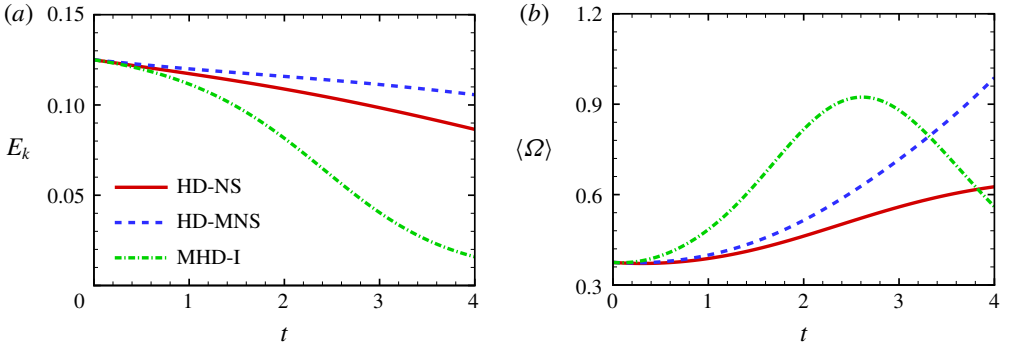

FIGURE 3. (Colour online) Temporal evolution of the volume-averaged (*a*) total kinetic energy and (*b*) enstrophy in cases HD-NS, HD-MNS and MHD-I.

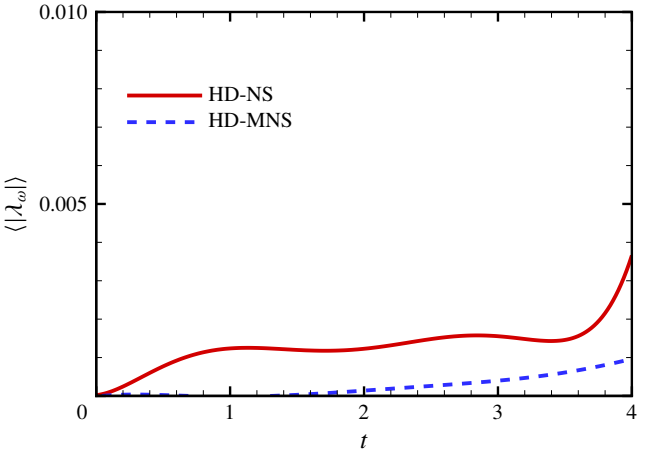

FIGURE 4. (Colour online) Temporal evolution of the volume-averaged VSF deviation in cases HD-NS and HD-MNS.

as $\langle|\lambda_\omega|\rangle \approx 10\,\%$ (Yang & Pullin 2010) owing to the breakdown of Helmholtz's theorem (also see figure 2). These observations support the frozen-in nature of the VSF in the virtual velocity of the modified fluid flow, so we can accurately track vortex surfaces in some non-ideal flows. We remark that the singular virtual velocity at vorticity nulls has been smoothed in the numerical implementation described in § 4.1, so the modified fluid flow in case HD-MNS has a globally smooth virtual velocity everywhere.

Moreover, the evolutions of VSF isosurfaces of $\hat{\phi}_v = 0.5$ in HD-NS and HD-MNS are shown in figure 5, where the normalized VSF $\hat{\phi}_v$ for further improving the time coherence in VSF visualization (see Peng & Yang 2018) is implicitly determined via $\hat{M}(\hat{\phi}_v = \varphi, t) = \hat{M}(\phi_{v0} = \varphi, t = 0)$. This normalization is performed by searching the isocontour values $\hat{\phi}_v = \varphi$ at a given time t and ϕ_{v0} at $t = 0$ which correspond to the same fluid mass $\hat{M}$. The solid lines are vortex lines integrated from points on the surfaces, and they are attached on the VSF isosurfaces. This observation also indicates very small deviations in both VSF calculations.

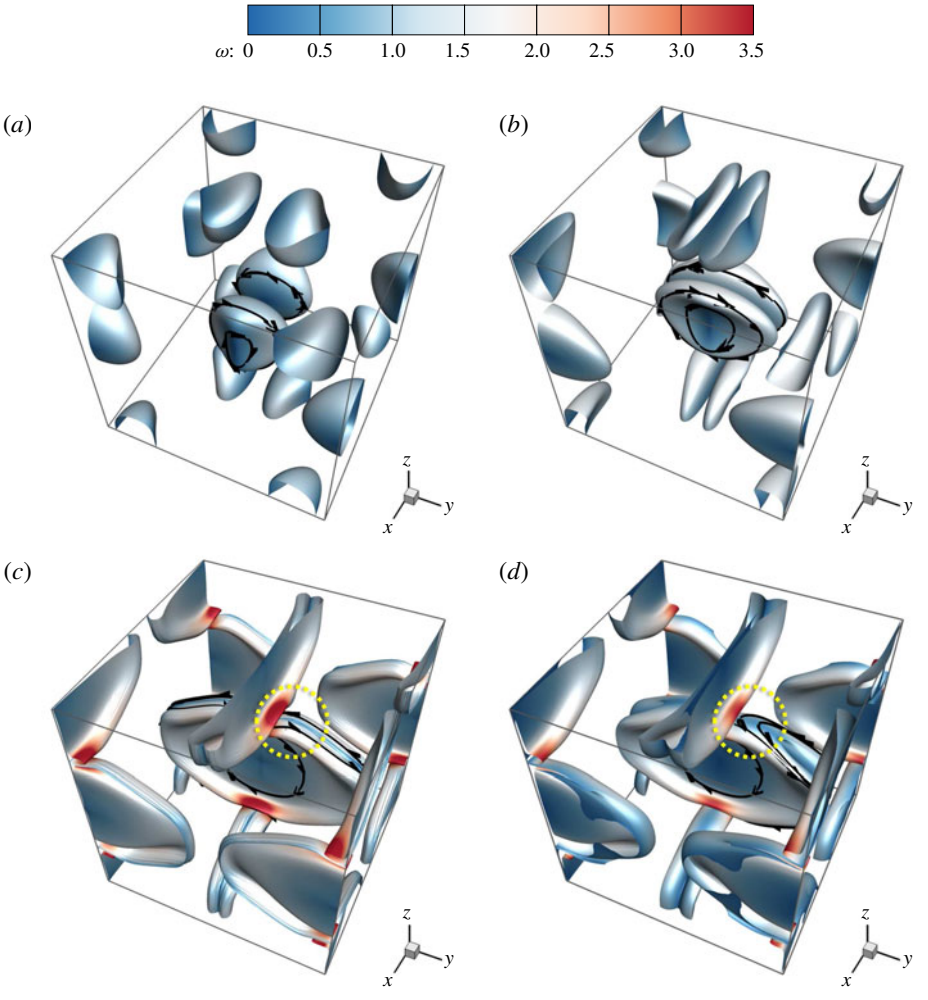

FIGURE 5. (Colour online) Temporal evolution of the VSF isosurface of $\hat{\phi}_v = 0.5$ in case HD-NS or HD-MNS at $Re = 100$. Some vortex lines are integrated and plotted on the isosurfaces colour-coded by ω. (*a*) HD-MNS, $t = 1$, (*b*) HD-MNS, $t = 2$, (*c*) HD-MNS, $t = 4$, (*d*) HD-NS, $t = 4$. The topological difference of the vortex lines in real TG flow (HD-NS) and modified TG flow (HD-MNS) is highlighted in yellow dotted circles in (*c*,*d*).

5.2. *Reconnection of vortex lines*

The geometry and topology in the evolution of vortex surfaces are important for characterizing flow transition in general and vortex reconnection (Kida & Takaoka 1994) in particular. The vortex reconnection in the transition in both incompressible and compressible TG flows at a range of *Re* has been extensively investigated in Yang & Pullin (2011) and Peng & Yang (2018). The typical initial VSF isosurfaces with (4.6) are a pair of ellipsoid-like blobs. As shown in figure 5, the vortex surfaces are extracted as the VSF isosurface $\hat{\phi} = 0.5$ colour-coded by $0 \leqslant \omega \leqslant 3.5$ from blue to red. The vortex pair approach each other and are flattened in the evolution, and then they merge together with significant vorticity amplification at surface edges, signalling incipient vortex reconnection.

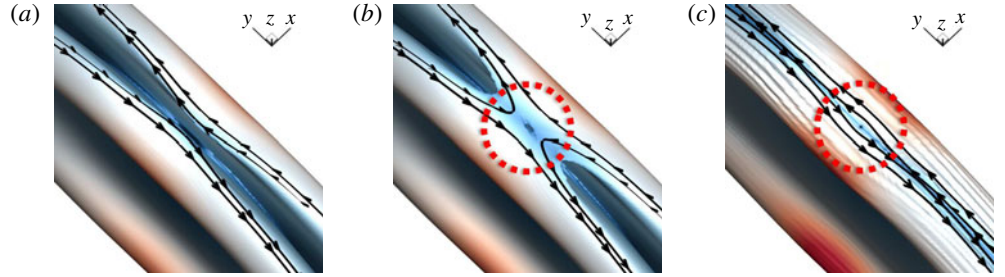

FIGURE 6. (Colour online) Close-up view of the VSF isosurface of $\hat{\phi}_v = 0.5$ near the vorticity null and the incipient reconnection time. Some vortex lines are integrated and plotted on the isosurfaces colour-coded by $0 \leqslant \omega \leqslant 3.5$. (*a*) HD-NS, $t = 3.6$, (*b*) HD-NS, $t = 3.65$, (*c*) HD-MNS, $t = 3.65$. The topological difference of the vortex lines in real TG flow (HD-NS) and modified TG flow (HD-MNS) is highlighted in red dotted circles in (*b*,*c*).

Before the vortex reconnection, the geometry of vortex surfaces and the topology of vortex lines in cases HD-NS and HD-MNS are very similar, so the VSF isosurfaces in HD-NS are not shown. During the vortex reconnection, the topology of vortex lines in HD-NS and HD-MNS is very different, as highlighted in the yellow dotted circle in figure 5(*c*,*d*). To further investigate the detailed process of the vortex reconnection, we zoom in on the VSF isosurfaces of $\hat{\phi}_v = 0.5$ around their incipient reconnection time $t \approx 3.65$ in figure 6. The vortex reconnection is expected to occur on the symmetric planes of the periodic cube in case HD-NS, e.g. the vortex lines reconnect with the opposite vortex lines at the y–z plane at $x = \pi$. We observe that the topology of vortex lines changes in the vicinity of the vorticity null highlighted in the red dotted circle in figure 6(*b*). In contrast, the topology of vortex lines in HD-MNS near $t = 3.65$, e.g. from $t = 3.6$ to $t = 3.7$ (not shown), is invariant in figure 6(*c*), and the vortex lines with opposite directions along the y–z plane at $x = \pi$ are almost parallel to each other. Thus the reconnection of vortex lines does not occur in the modified fluid flow. We remark that the approaching VSF isosurfaces appear to merge, but theoretically in between there should be a decreasing gap, which is not resolved under the present VSF grid resolution.

Based on the VSF evolution, we quantify the incipient vortex reconnection using the vorticity flux through the symmetric plane between a pair of approaching vortex surfaces (see Peng & Yang 2018). Without loss of generality, we consider the vorticity flux through the x–z symmetric plane at $y = \pi$ between a pair of merging VSF isosurfaces of $\hat{\phi}_v = 0.5$. During the vortex reconnection, vortex lines are cut in the y-direction and reconnected in the x-direction. The vorticity fluxes through the x–z plane at $y = \pi$ and through the y–z plane at $x = \pi$ are defined as $\Phi_y \equiv \int_{\mathcal{S}_y} \omega_y \, \mathrm{d}\mathcal{S}$ and $\Phi_x \equiv \int_{\mathcal{S}_x} \omega_x \, \mathrm{d}\mathcal{S}$, respectively. Here, $\mathcal{S}_y$ and $\mathcal{S}_x$ are the regions enclosed by a half of the VSF contour line $\hat{\phi}_v = 0.5$ and the x–y plane at $z = \pi$ on their corresponding symmetric planes. The temporal evolution of the vorticity fluxes in figure 7 shows that Φ_y decreases and Φ_x increases significantly around $t = 2.6$ in case HD-NS, which indicates that the reconnection of vortex lines occurs as the exchange of vorticity directions through symmetric planes. In contrast, Φ_x and Φ_y in HD-MNS are conserved during the evolution.

This quantification implies that the reconnection of vortex lines is prohibited in the modified fluid flow in HD-MNS. In other words, the vortex lines in a non-ideal,

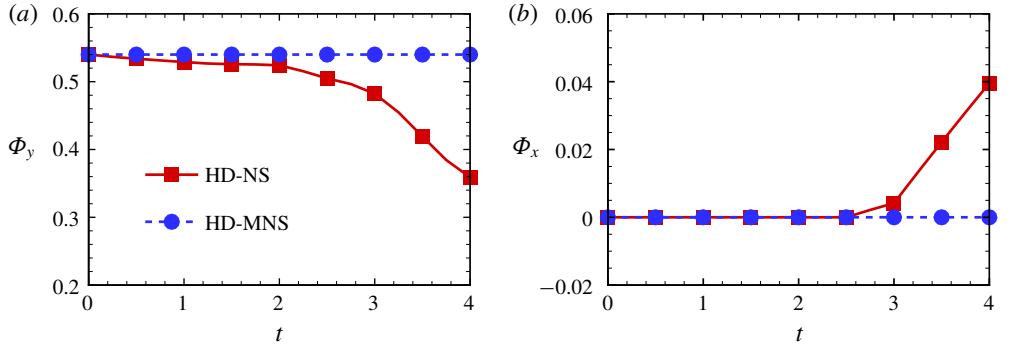

FIGURE 7. (Colour online) Temporal evolution of the vorticity fluxes through symmetric planes. (*a*) Φ_y and (*b*) Φ_x.

dissipative flow can still have topological invariance. This result agrees with (2.12) for the virtual conservation of vorticity flux, (2.19) for the virtual conservation of helicity and the visualization of vortex lines in figures 5 and 6. In the framework of the virtual velocity, the reconnection of vortex lines is triggered by non-vanishing $\boldsymbol{F}_{\parallel}$ in NS equations or vorticity nulls.

6. VSF evolution in MHD TG flows

6.1. *Spurious deformation of vortex surfaces*

In MHD TG flows, the non-ideal force term $\boldsymbol{F} = \boldsymbol{F}_{\nu} + \boldsymbol{F}_{L}$ in MHD equations (4.3) includes the viscous term $\boldsymbol{F}_{\nu} = \nu\nabla^2\boldsymbol{u}$ and the Lorentz force term $\boldsymbol{F}_{L} = \boldsymbol{j} \times \boldsymbol{b}$. As discussed in § 5 and Yang & Pullin (2010), the viscous effect in HD TG flows is negligible on vortex evolution with high Re until significant vortex reconnection. By contrast, the non-ideal effect in MHD TG flows, dominated by the Lorentz force term, can have an impact on tracking vortex surfaces.

For case MHD-S, the vorticity in the reduced MHD equations (4.4) has an exact solution

$$\boldsymbol{\omega}(\boldsymbol{x}, t) = \boldsymbol{\omega}_0 \mathrm{e}^{-\nu t}, \tag{6.1}$$

where $\boldsymbol{\omega}_0$ denotes the initial vorticity. This solution indicates that the geometry and topology of vortex lines are invariant in MHD-S. Nonetheless, if the VSF is calculated as (3.3) driven by the physical velocity $\boldsymbol{u}$ using the two-time method in MHD-S, which is similar to dye visualization in experiments, we find that the evolving VSF isosurface has significant geometrical and topological changes. In figure 8, VSF isosurfaces evolve from initial ellipsoids, and then they appear to collide and merge with significant deformation. This observation contradicts the steady vortex lines implied in (6.1).

This inconsistency implies that convecting VSF along the physical velocity in MHD flows with strong non-ideal forces can result in spurious deformation of vortex surfaces. Moreover, the VSF solution in MHD-S is still accurate with $\langle|\lambda_{\omega}|\rangle < 1\,\%$ as the perfect attachment of vortex lines in figure 8. Although the deviation of VSF solutions owing to non-ideal forces is corrected in the two-time method, one VSF solution can evolve into another VSF solution.

The spurious deformation of VSF isosurfaces manifests the non-uniqueness of VSF solutions, but it can be eliminated by convecting the VSF along the virtual

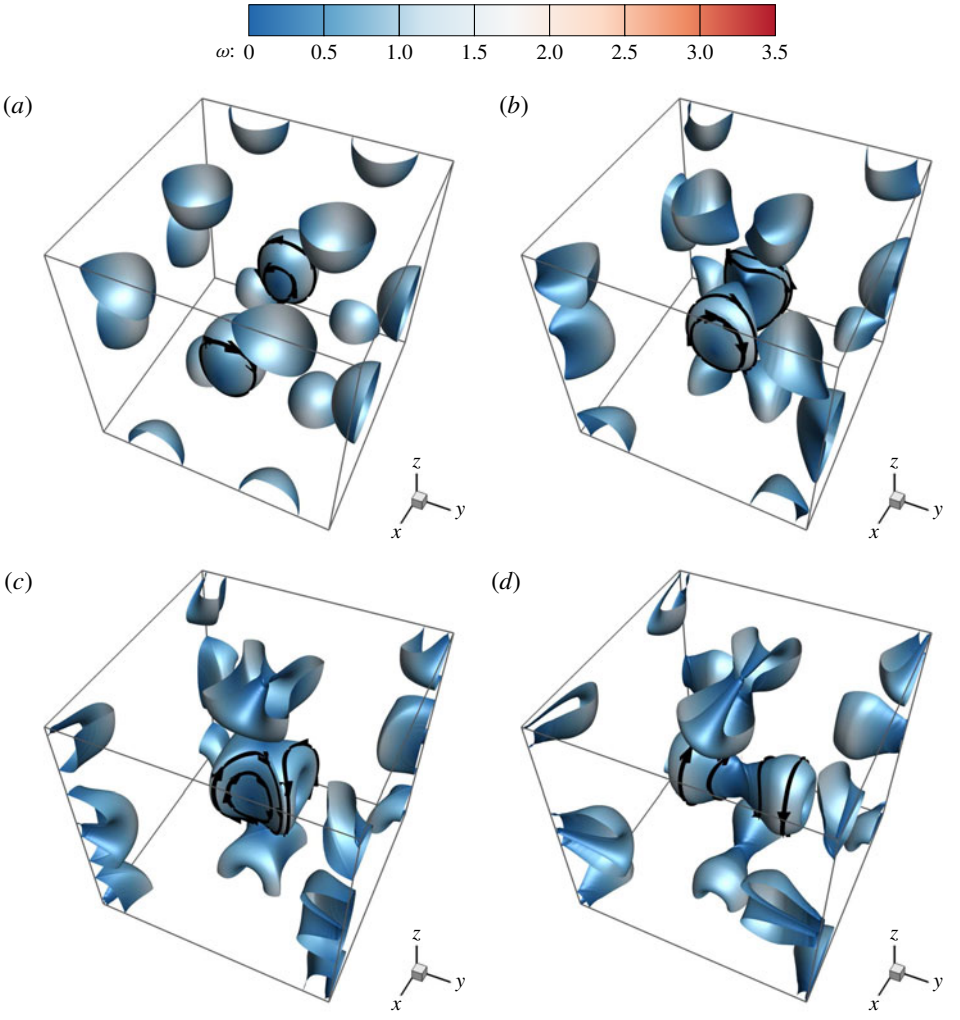

FIGURE 8. (Colour online) The spurious deformation of vortex surfaces in non-ideal flows is illustrated by the evolving VSF isosurface of $\hat{\phi}_v = 0.5$ in case MHD-S at $Re = 100$. Some vortex lines are integrated and plotted on the isosurfaces colour-coded by ω. (*a*) $t = 0$, (*b*) $t = 1$, (*c*) $t = 2$, (*d*) $t = 3$.

velocity as in case MHD-SV. For the steady MHD TG flow with $\nu = \eta = 0$, the drift velocity has the exact solution $\boldsymbol{v}_d = -\boldsymbol{u}$, then the virtual VSF transport (3.5) with the vanishing virtual velocity $\boldsymbol{v} = 0$ is reduced to the steady VSF equation $\partial\phi_v/\partial t = 0$. In other words, the motion driven by the drift velocity cancels the spurious deformation induced by non-ideal forces, so that we can obtain the vortex surfaces with invariant geometry and topology in MHD-SV, which agrees with the theoretical solution (6.1).

6.2. *Tracking vortex surfaces in the approximate virtual velocity*

As discussed in § 4.4, when the explicit virtual velocity does not exist, we can still seek a good approximate virtual velocity in the non-ideal flows in which $\boldsymbol{F}$ has a preferential normal alignment with $\boldsymbol{\omega}$. For the insulating MHD TG flow in

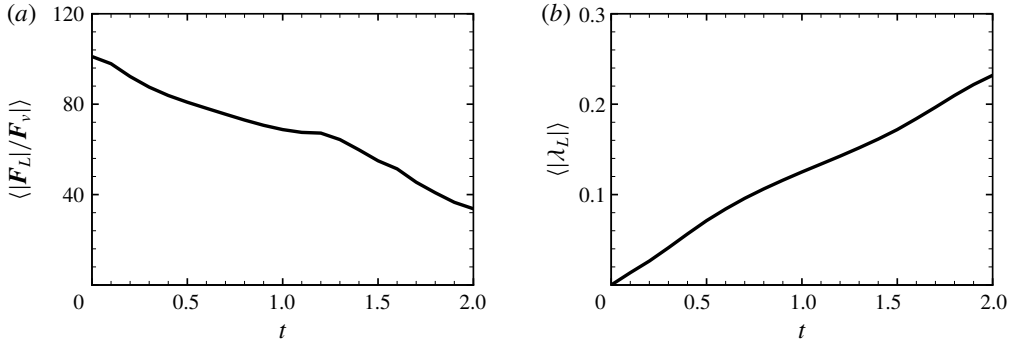

FIGURE 9. Temporal evolution of volume-averaged quantities in the insulating MHD TG flow at $Re = 100$. (*a*) Ratio of the magnitudes of Lorentz force term to viscous term. (*b*) Preferential normal alignment between $\boldsymbol{F}_L$ and $\boldsymbol{\omega}$.

case MHD-I, both $\boldsymbol{F}_v$ and $\boldsymbol{F}_L$ are perpendicular to $\boldsymbol{\omega}$ at the initial time. On average, $|\boldsymbol{F}_L|$ is at least an order of magnitude greater than $|\boldsymbol{F}_v|$ at $0 \leqslant t \leqslant 2$ in figure 9(*a*), so the Lorentz force dominates the non-ideal force and then we neglect the viscous effect in $\boldsymbol{F}$ during the time interval of interest.

The preferential normal alignment between $\boldsymbol{F}_L$ and $\boldsymbol{\omega}$ is quantified by the volume average of

$$\lambda_L \equiv \frac{\boldsymbol{F}_L \cdot \boldsymbol{\omega}}{|\boldsymbol{F}_L|\,|\boldsymbol{\omega}|}. \tag{6.2}$$

The growing $\langle|\lambda_L|\rangle$ in figure 9(*b*) implies that the preferential normal alignment is suppressed with time, but $\langle|\lambda_L|\rangle < 0.25$ still maintains at a relatively small value. Thus we consider the approximate virtual velocity (2.37) as

$$\boldsymbol{v} = \boldsymbol{u} + \frac{\boldsymbol{\omega} \times \boldsymbol{F}_L}{\omega^2}, \tag{6.3}$$

and we will demonstrate that this approximate virtual velocity can effectively reduce the spurious deformation of vortex surfaces discussed in § 6.1 to improve the vorticity flux conservation in the virtual evolution.

Temporal evolutions of VSF isosurfaces $\phi_v = 0.5$ in cases MHD-I and MHD-IV at $Re = 100$ are shown in figures 10 and 11, respectively. The VSF deviation $\langle|\lambda_\omega|\rangle < 1\,\%$ is very small for both cases at $0 \leqslant t \leqslant 2$, and vortex lines almost lie on the VSF isosurfaces. We observe that the evolutions of vortex surfaces in the two cases display significant differences in both evolutionary topology and geometry.

In MHD-I, the VSF is primarily convected by the physical velocity $\boldsymbol{u}$ in the two-time method. Comparing with the VSF evolution in HD TG flows in figure 5, we observe in figure 10 that long tubular structures are stretched out from the approaching vortex surfaces at $t = 1$ under the influence of strong non-ideal Lorentz force. Then these structures are shortened at $t = 1.5$ and $t = 2$. Furthermore, the two approaching vortex surfaces do not merge at $t = 2$.

In MHD-IV, the VSF is convected by the approximate virtual velocity (6.3). The evolution of vortex surfaces in figure 11 is similar to that in HD TG flows in figure 5. The approaching surfaces are only flattened at $0 \leqslant t \leqslant 1$ without the small-scale protruding structures in figure 10(*b*). As discussed in § 6.1, the protruding structures appear to be spurious deformation owing to the non-uniqueness of VSF solutions.

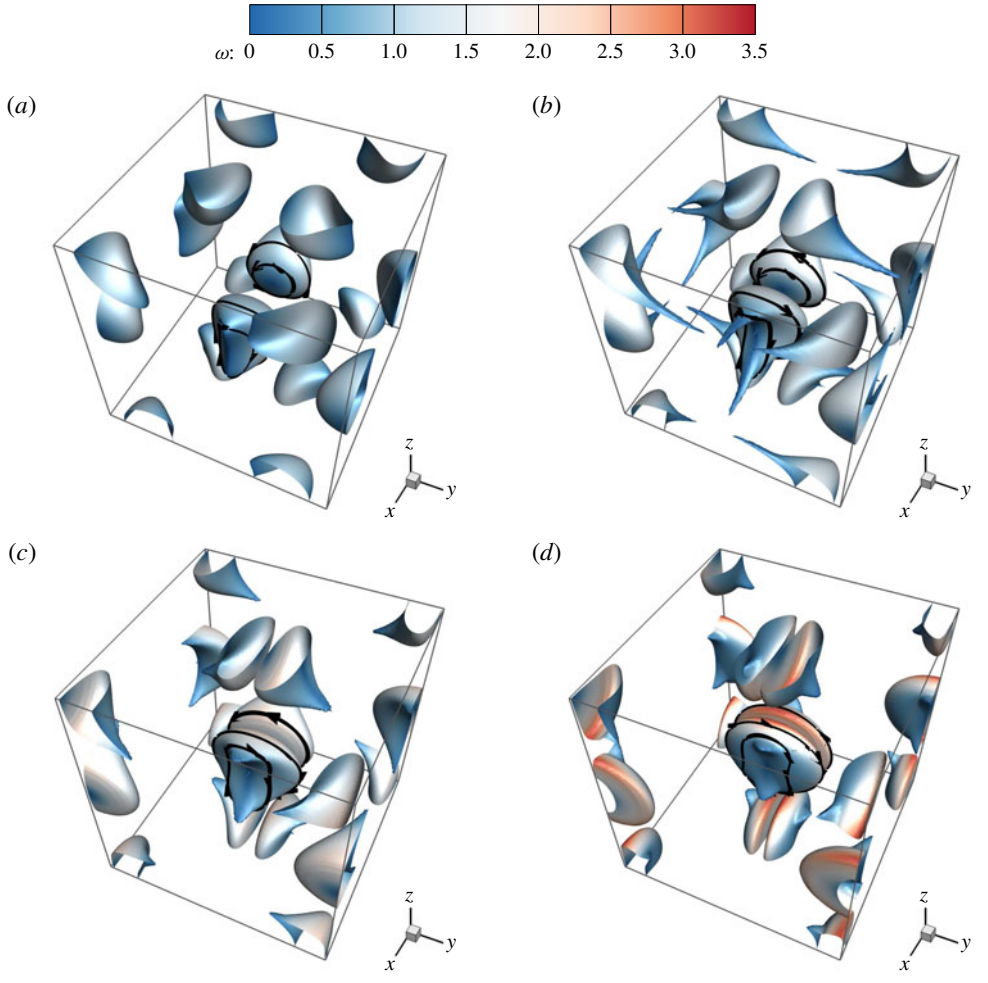

FIGURE 10. (Colour online) Temporal evolution of the VSF isosurface of $\hat{\phi}_v = 0.5$ in case MHD-I at $Re = 100$, where the VSF is convected by the physical velocity. Some vortex lines are integrated and plotted on the isosurfaces colour-coded by ω. (*a*) $t = 0.5$, (*b*) $t = 1.0$, (*c*) $t = 1.5$, (*d*) $t = 2.0$.

In figure 11(*b*), they are eliminated by incorporating the virtual velocity in the tracking of vortex surfaces. After $t = 1$, the two vortex surfaces merge together and the reconnection of vortex lines occurs around $t = 1.5$.

6.3. *Virtual conservation of vorticity flux*

Virtual Helmholtz's theorem (2.12) suggests that the vorticity flux is conserved in tracking vortex surfaces along a smooth virtual velocity (also see figure 2). Without loss of generality, the evolution of vorticity flux Φ_y through the x–z symmetric plane at $y = \pi$ is shown in figure 12. In MHD-IV, Φ_y is almost conserved before $t = 1$ as the VSF isosurfaces have not touched the vorticity nulls at the centre in figure 11(*b*). After $t = 1$, the rapid decay of Φ_y signals the incipient reconnection of vortex lines in figure 11(*c*). This trend is consistent with the decaying of Φ_y in HD TG flows

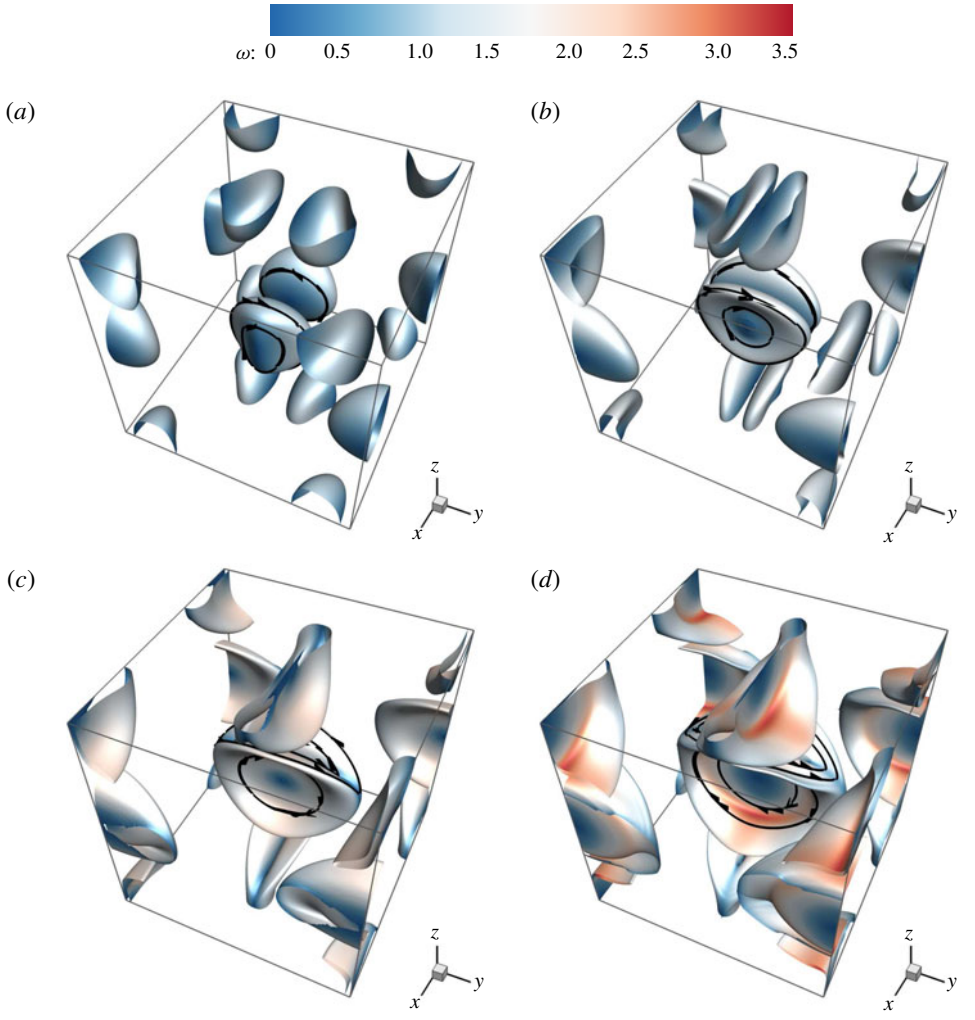

FIGURE 11. (Colour online) Temporal evolution of the VSF isosurface of $\hat{\phi}_v = 0.5$ in case MHD-IV at $Re = 100$, where the VSF is convected by the virtual velocity. Some vortex lines are integrated and plotted on the isosurfaces colour-coded by ω. (*a*) $t = 0.5$, (*b*) $t = 1.0$, (*c*) $t = 1.5$, (*d*) $t = 2.0$.

in figure 7(*a*). By contrast, Φ_y in MHD-I is not conserved throughout the entire evolution.

Figure 13 displays the boundaries of VSF isosurfaces in MHD-I (grey thin lines) and MHD-IV (black thick lines) on the x–z symmetric plane at $y = \pi$. At $t = 0$, the approaching motion of the vortex pair driven by the virtual velocity $\boldsymbol{v} \approx 2\boldsymbol{u}$ is much faster than that driven by $\boldsymbol{u}$. Then the vortex pair in MHD-IV is also flattened and merged more quickly than that in MHD-I. We observe that the VSF contour lines in MHD-IV can capture the regions with significant vorticity intensification, whereas the contour lines in MHD-IV do not well coincide with the regions with growing Φ_y. This observation supports that better conservation of Φ_y is achieved in MHD-IV than in MHD-I before the merging of vortex surfaces.

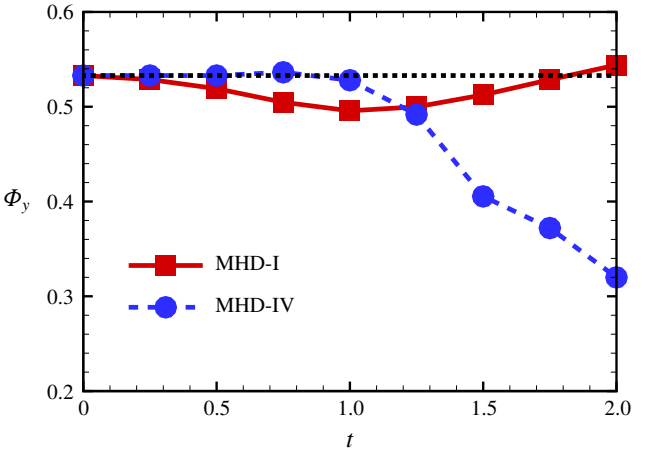

FIGURE 12. (Colour online) Temporal evolution of vorticity flux Φ_y through the x–z symmetric plane at $y=\pi$. The dotted line denotes the value of Φ_y at $t=0$.

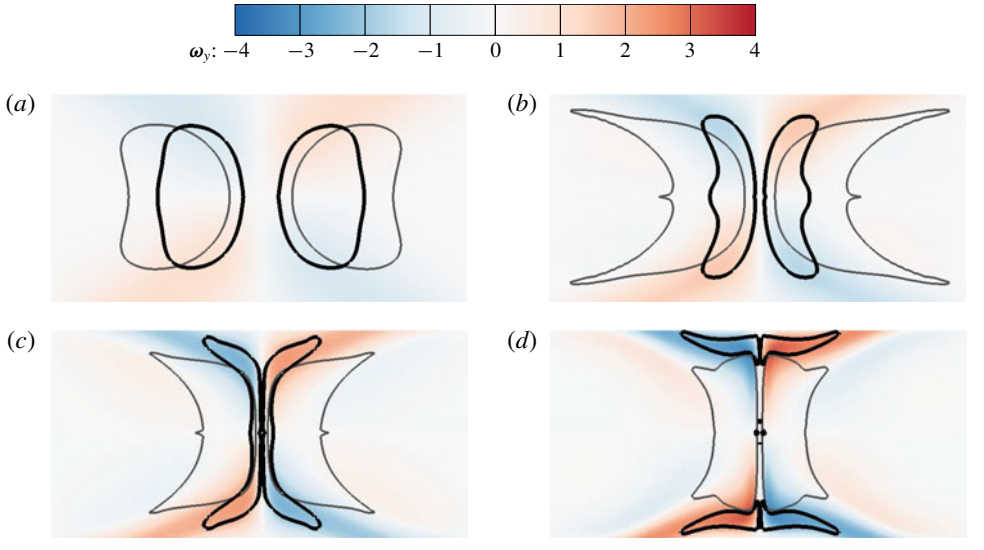

FIGURE 13. (Colour online) Comparison of the VSF evolutions convected by the physical velocity in case MHD-I and convected by the virtual velocity in case MHD-IV on the x–z symmetric plane within $0\leqslant x\leqslant 2\pi$ and $\pi/2\leqslant z\leqslant 3\pi/2$ at $y=\pi$. Thick black and thin grey lines are contour lines of $\hat{\phi}_v=0.5$ in MHD-IV and MHD-I, respectively. The contour is colour-coded by ω_y. (*a*) $t=0.5$, (*b*) $t=1.0$, (*c*) $t=1.5$, (*d*) $t=2.0$.

The similarities on the evolutionary geometry of vortex surfaces in figures 5 and 10 indicate that the vortex dynamics in HD TG flow and insulating MHD TG flow appears to be essentially the same before the vortex reconnection, but the incipient reconnection of vortex surfaces with larger $\boldsymbol{v}_d$ in MHD-IV occurs earlier than that in HD-NS. Since vortex lines are stretched during the vortex reconnection (see Yang & Pullin 2011), the total energy or enstrophy in the insulating MHD TG flow is smaller or larger than that in the HD TG flow in figure 3. Therefore, the time for the

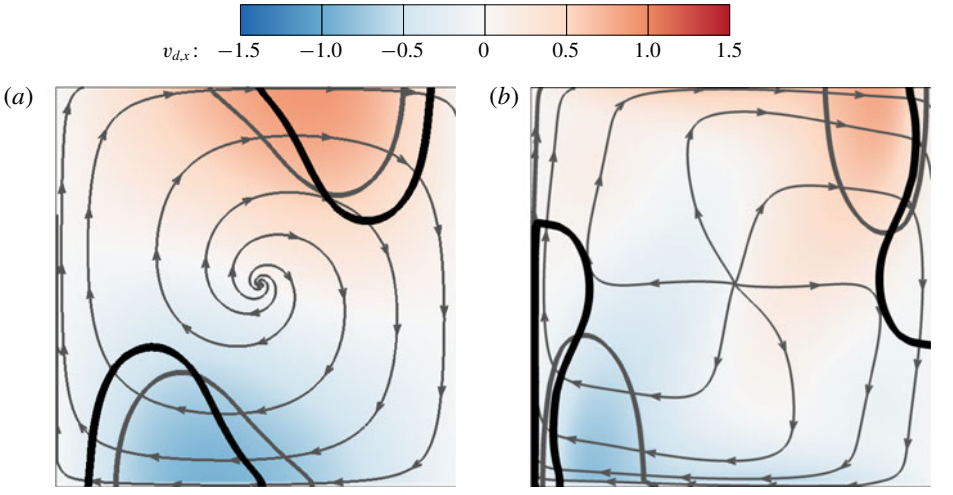

FIGURE 14. (Colour online) Comparison of the VSF evolutions convected by the physical velocity in case MHD-I and convected by the virtual velocity in case MHD-IV with streamlines of the virtual velocity on the x–y symmetric plane within $0 \leqslant x \leqslant \pi$ and $0 \leqslant y \leqslant \pi$ at $z = \pi$. Thick black and thin grey lines are contour lines of $\hat{\phi}_v = 0.5$ in MHD-IV and MHD-I, respectively. The contour is colour-coded by $-1.3 \leqslant v_{d,x} \leqslant 1.3$ from blue to red. (*a*) $t = 0.5$, (*b*) $t = 1.5$.

turbulent transition at larger Re or the potential finite-time singularity in the inviscid limit in MHD TG flows (see Lee *et al.* 2009) is earlier than that in corresponding HD flows (see Brachet *et al.* 1983).

In addition, the boundaries of VSF isosurfaces in MHD-I (grey thin lines) and MHD-IV (black thick lines) on the x–y symmetric plane at $z = \pi$ are shown in figure 14. The acceleration of vortex motion in the virtual Lagrangian view is depicted by the contour of the x-component of $\boldsymbol{v}_d$. The outward spiral streamlines of the virtual velocity sweep vortex surfaces towards impermeable planes faster than the closed streamlines (not shown) of the physical velocity.

In non-ideal flows, the results in this section demonstrate that tracking vortex surfaces in the virtual velocity appears to be more physically reasonable than tracking in the physical velocity. First, tracking vortex surfaces in the physical velocity can cause spurious deformation in flows with strong non-ideal forces, whereas tracking in the virtual velocity can eliminate such an artifact. Second, tracking in the virtual velocity has better conservation of vorticity flux and other vorticity-related quantities than tracking in the physical velocity.

7. Conclusions

It appears that vortex surfaces cannot be exactly tracked in flows with viscous, baroclinic and non-conservative body forces, because Helmholtz's vorticity theorem breaks down in non-ideal flows. However, we show that the vortex surfaces can still be tracked along a virtual circulation-preserving velocity, instead of the physical velocity, in non-ideal flows.

Theoretically, tracking vortex surfaces in the virtual velocity is based on the extension of the classical vorticity-related conservation theorems in ideal flows to non-ideal flows, e.g. virtual Helmholtz's theorem. We propose the sufficient condition

for applying the virtual conservation theorems to a vortex surface moving with a globally smooth virtual velocity. In a finite region where the vortex surface sweeps, the vorticity-parallel component of the non-ideal force should be irrotational and the local vorticity does not vanish. Although the existence and uniqueness of the globally smooth virtual velocity are not ensured in general flows, we provide several examples for uniquely determining the explicit virtual velocity in some non-ideal flows.

Numerically, tracking vortex surfaces is implemented by reformulating the existing VSF framework with the virtual velocity. The VSF is convected by the virtual velocity as a Lagrangian passive scalar, and evolving vortex surfaces are extracted from the VSF at a particular isocontour level.

We demonstrate that incorporating the virtual velocity with the VSF is useful for vortex tracking in non-ideal flows in two examples of three-dimensional TG flows at a low Reynolds number $Re = 100$. First, we propose a modified HD flow with a viscous-like diffusion term which is orthogonal to the vorticity without singularity, so that we can obtain an explicit virtual velocity to accurately track vortex surfaces in time. We find that the modified HD TG flow is less dissipative than the real TG flow, and prohibits reconnection of vortex lines. The reconnection degree is quantified by the exchange of vorticity fluxes through two orthogonal cross-sections of approaching closed vortex surfaces. The vorticity fluxes change significantly around $t = 2.6$ in the real HD TG flow, signalling incipient vortex reconnection, whereas they are conserved in the modified HD TG flow, consistent with virtual Helmholtz's theorem.

Second, we can obtain an approximate virtual velocity in a non-ideal flow with the preferential normal alignment between the non-ideal force and vorticity. By using the approximate virtual velocity, we track vortex surfaces in an insulating MHD TG flow with strong non-ideal forces. Compared with vortex tracking in the physical velocity, we find that incorporating the approximate virtual velocity into vortex tracking can significantly improve the conservation of vorticity flux by eliminating spurious deformation of vortex surfaces induced by the Lorentz force. Moreover, the vortex dynamics in HD and insulating MHD TG flows appears to be essentially the same, i.e. two initial vortex blobs first approach each other and then they merge at the symmetric plane as vortex reconnection. On the other hand, the approaching motion of the vortex pair in MHD flows is accelerated in the virtual velocity by incorporating the effect of the Lorentz force, so the reconnection time around $t = 1$ in the MHD TG flow is earlier than that in the HD TG flow.

In the present study, the discussion of the virtual velocity is restricted to several simple non-ideal flows. It is worth developing a relatively accurate and efficient method to calculate the approximate virtual velocity in general three-dimensional flows, and regularize the singular virtual velocity at vorticity nulls. From the Lagrangian view, the VSF with the virtual velocity can be used to track vortex surfaces and investigate the vortex dynamics in strong non-ideal flows, such as in hypersonic flows, combustion and MHD turbulence. Furthermore, both the virtual velocity and VSF can be generalized with their counterparts in the electromagnetic field for various non-ideal systems.

Acknowledgements

Y.Y. is grateful for stimulating discussions with J.-Z. Zhu on the idea of virtual velocity and virtual frozen-in vorticity, and thanks W.-D. Su, J.-Z. Wu and Y. Zhao for helpful comments. Numerical simulations were carried out on the TH-2A supercomputer in Guangzhou, China. This work was supported in part by the National Natural Science Foundation of China (grant nos. 11522215, 91541204 and 11521091).

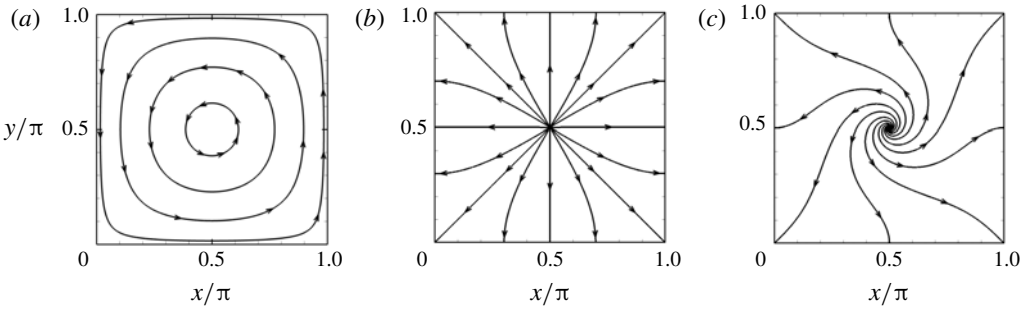

FIGURE 15. Streamlines of (*a*) physical velocity $\boldsymbol{u}$, (*b*) drift velocity $\boldsymbol{v}_d$ and (*c*) virtual velocity $\boldsymbol{v}$ in a two-dimensional HD TG flow with $\nu = 1$.

Supplementary material

Supplementary material is available at https://doi.org/10.1017/jfm.2018.1014.

Appendix A. Examples of the explicit virtual velocity

A.1. *Two-dimensional TG flow*

We illustrate the physical meaning of the virtual velocity in a two-dimensional HD TG flow. This flow in a periodic square domain of side 2π has an exact solution of $\boldsymbol{u}$ as

$$\left.\begin{aligned} u_x &= \mathrm{e}^{-2\nu t}\sin x\cos y,\\ u_y &= -\mathrm{e}^{-2\nu t}\cos x\sin y. \end{aligned}\right\} \tag{A 1}$$

In this two-dimensional flow, the vorticity has only one component: $\omega_z = 2\mathrm{e}^{-2\nu t}\sin x\sin y$. Thus (2.32) is satisfied with $\boldsymbol{F} = \nu\nabla^2\boldsymbol{u}$ and the virtual velocity is obtained from (2.37) as

$$\left.\begin{aligned} v_x &= \mathrm{e}^{-2\nu t}\sin x\cos y - \nu\cot x,\\ v_y &= -\mathrm{e}^{-2\nu t}\cos x\sin y - \nu\cot y. \end{aligned}\right\} \tag{A 2}$$

Streamlines for the physical velocity, drift velocity and virtual velocity within a impermeable cell enclosed by heteroclitic orbits connecting the saddle points of $\boldsymbol{u}$ are plotted in figure 15. The streamlines of $\boldsymbol{u}$ are closed curves, and the heteroclitic orbits are $x = 0,\ \pi$ and $y = 0,\ \pi$. The virtual velocity is not divergence-free, so its streamlines have a source at the centre of each cell. The drift velocity goes to infinity at the heteroclitic orbits.

The transport equation for vorticity in terms of $\boldsymbol{u}$ can be re-expressed in terms of the virtual velocity as

$$\frac{\mathrm{D}_v\omega_z}{\mathrm{D}_v t} = -\omega_z\left(\frac{\partial v_x}{\partial x} + \frac{\partial v_y}{\partial y}\right). \tag{A 3}$$

On a virtual particle travelling with the virtual velocity, the vorticity magnitude decays with time as

$$\omega_z = 2\sin x\sin y\exp[-\nu(\csc^2 x + \csc^2 y)t]. \tag{A 4}$$

The path of each particle released at the initial time at somewhere with $\omega \neq 0$ is an outward spiral towards the heteroclitic orbits of $\boldsymbol{u}$.

For any loop $\mathcal{C}$ without passing the heteroclitic orbits, the vorticity flux $\int_{\mathcal{S}}\omega_z\,\mathrm{d}\mathcal{S}$ is conserved where $\mathcal{S}$ is enclosed by $\mathcal{C}$. This can be interpreted as that the cross-section

of a vortex tube oriented in the z-direction expands in the flow evolution from the virtual Lagrangian view. The vortex will merge with others in adjacent impermeable cells when $\mathcal{C}$ reaches a heteroclitic orbit, and in the meantime virtual Helmholtz's theorem breaks down owing to the singular virtual velocity.

A.2. *Integrable ABC flow*

We argue that (2.32) is a sufficient condition for the existence of a non-trivial smooth virtual velocity. In other words, the exact solution of $\boldsymbol{v}$ can still exist even in some particular flows with $\nabla \times \boldsymbol{F}_{\parallel} \neq 0$, e.g. the integrable ABC flow.

The viscous ABC flow has an exact solution:

$$\boldsymbol{u} = \boldsymbol{\omega} = (A \sin z + C \cos y, B \sin x + A \cos z, C \sin y + B \cos x), \tag{A 5}$$

with $A = A_0 \exp(-\nu t)$, $B = B_0 \exp(-\nu t)$ and $C = C_0 \exp(-\nu t)$, and constants A_0, B_0 and C_0. The vorticity is parallel to velocity in this Beltrami-type flow. The non-ideal force term $\boldsymbol{F} = \nu \nabla^2 \boldsymbol{u}$ has $\nabla \times \boldsymbol{F}_{\parallel} = -\nu \boldsymbol{u} \neq 0$. The vorticity equation is $\partial \boldsymbol{\omega}/\partial t = \nu \nabla^2 \boldsymbol{\omega}$, so the flow decays in time without changing geometry and topology of vortex lines.

In such a simple viscous flow, we only find an exact solution of $\boldsymbol{v}$ when the ABC flow is integrable with $B = C = 0$ or any other two constants are vanishing. Then the flow becomes two-component as

$$\boldsymbol{u} = \boldsymbol{\omega} = (A \sin z, A \cos z, 0), \tag{A 6}$$

so that we can determine a non-trivial Ψ in (2.26) as

$$\Psi = \nu A (x \sin z + y \cos z) \tag{A 7}$$

from the constraint (2.25)

$$A \sin z \frac{\partial \Psi}{\partial x} + A \cos z \frac{\partial \Psi}{\partial y} = \nu A^2. \tag{A 8}$$

The corresponding two-component drift velocity

$$\boldsymbol{v}_d = (\nu \cos z (x \cos z - y \sin z), \nu \sin z (-x \cos z + y \sin z), 0) \tag{A 9}$$

is exactly normal to $\boldsymbol{u}$ and $\boldsymbol{\omega}$ on each x–y planar vortex surface. The virtual transport of vorticity does not change the geometry and topology of vortex lines and surfaces from $\boldsymbol{v}_d \cdot \nabla \boldsymbol{\omega} = 0$, $\boldsymbol{\omega} \cdot \nabla \boldsymbol{v}_d = 0$ and $\boldsymbol{v}_d \cdot \nabla \phi_v = 0$, where initial ϕ_v is an arbitrary smooth function of z. This observation agrees with the exact solution (A 5).

A.3. *Incompressible Schrödinger flow*

The ISF is an artificial non-ideal flow which shares some physical features of superfluids (see Chern *et al.* 2016). As favoured in computer graphics for fluid motion, the calculation of the ISF is computationally efficient, and the flow visualization of the ISF can display striking interactions of vortex filaments. Next we will briefly review the derivation of the ISF equations in a regular vector form, and demonstrate that the ISF has an explicit virtual velocity. Detailed formulation of the ISF in the forms of exterior calculus and quaternion can be found in Chern (2017).

The ISF framework reveals some underlying relations between fluid dynamics and quantum physics. Similar exploration dates back to Madelung (1927), who found that the Schrödinger equation can be transformed into two-dimensional compressible Euler equations, but the corresponding fluid flow is irrotational with very limited applications. In order to model more realistic vortical flows, Chern *et al.* (2016) proposed a two-component Schrödinger equation for incompressible flows. In terms of the two-component wave function

$$\boldsymbol{\psi} = (\psi_1, \psi_2) \quad \text{with } \psi_1 = a + \mathrm{i}b \text{ and } \psi_2 = c + \mathrm{i}d, \tag{A 10}$$

the ISF is governed by

$$\left.\begin{aligned} \mathrm{i}\hbar\frac{\partial \boldsymbol{\psi}}{\partial t} &= -\frac{\hbar^2}{2}\nabla^2\boldsymbol{\psi} + \widetilde{p}\boldsymbol{\psi}, \quad \boldsymbol{x} \in \mathcal{V},\ t > 0, \\ \langle \nabla^2\boldsymbol{\psi}, \mathrm{i}\boldsymbol{\psi}\rangle_{\mathbb{R}} &= 0, \quad \boldsymbol{x} \in \mathcal{V},\ t \geqslant 0, \\ \langle \boldsymbol{\psi}, \boldsymbol{\psi}\rangle_{\mathbb{R}} &= 1, \quad \boldsymbol{x} \in \mathcal{V},\ t \geqslant 0, \\ \frac{\partial \boldsymbol{\psi}}{\partial n} &= 0, \quad \boldsymbol{x} \in \partial\mathcal{V},\ t \geqslant 0, \end{aligned}\right\} \tag{A 11}$$

with $\mathcal{V} \subseteq \mathbb{R}^3$ and a constant $\hbar$. Here, $\langle\cdot\rangle_{\mathbb{R}}$ is defined as

$$\langle \boldsymbol{z}, \boldsymbol{\gamma}\rangle_{\mathbb{R}} \equiv \sum_{i=1}^{2}(x_i\alpha_i + y_i\beta_i), \quad \forall \boldsymbol{z} = (x_1 + \mathrm{i}y_1, x_2 + \mathrm{i}y_2),\ \boldsymbol{\gamma} = (\alpha_1 + \mathrm{i}\beta_1, \alpha_2 + \mathrm{i}\beta_2), \tag{A 12}$$

and the modified pressure $\widetilde{p}$ is determined by a Poisson equation

$$\nabla^2\widetilde{p} = \frac{\hbar}{2}[\langle \nabla^2(\nabla^2\boldsymbol{\psi}), \boldsymbol{\psi}\rangle_{\mathbb{R}} - \langle \nabla^2(\nabla^2\boldsymbol{\psi}), \nabla^2(\nabla^2\boldsymbol{\psi})\rangle_{\mathbb{R}}]. \tag{A 13}$$

Chern *et al.* (2016) argued that the computational cost for numerically solving (A 11) is much less than that for regular NS equations.

To visualize fluid motion, the wavefunction (A 10) can be converted into fluid velocity as

$$\boldsymbol{u} = \hbar\langle \nabla\boldsymbol{\psi}, \mathrm{i}\boldsymbol{\psi}\rangle_{\mathbb{R}} = \hbar(a\nabla b - b\nabla a + c\nabla d - d\nabla c). \tag{A 14}$$

This velocity field is driven by the 'Landau–Lifshitz force'

$$\boldsymbol{F} = -\frac{\hbar^2}{4}(\nabla^2\boldsymbol{s})\cdot\nabla\boldsymbol{s}, \tag{A 15}$$

where the 'spin vector' is defined as

$$\boldsymbol{s} = (s_1, s_2, s_3) \equiv (1 - 2c^2 - 2d^2, 2bc - 2ad, 2bd + 2ac), \tag{A 16}$$

and each component of $\boldsymbol{s}$ is a Clebsch potential of ISF. After some algebra, we obtain that the evolution equation of $\boldsymbol{u}$ in ISF is in the form of the NS momentum equation (2.2) along with $\nabla\cdot\boldsymbol{u} = 0$, $\Pi = \widetilde{p} + \hbar^2|\nabla\boldsymbol{s}|^2/8$ and (A 15).

The vorticity in the ISF can be expressed in terms of components of $\boldsymbol{s}$ as

$$\boldsymbol{\omega} = \frac{\hbar}{2}\frac{\nabla s_2 \times \nabla s_3}{s_1} = \frac{\hbar}{2}\frac{\nabla s_3 \times \nabla s_1}{s_2} = \frac{\hbar}{2}\frac{\nabla s_1 \times \nabla s_2}{s_3}, \tag{A 17}$$

then we find that $\boldsymbol{F}$ is orthogonal to $\boldsymbol{\omega}$ as (2.31) or $\boldsymbol{F}_{\parallel}=0$. Therefore, the evolution equation of $\boldsymbol{u}$ in the ISF has the same form as the MNS equation (2.35), and we obtain the explicit virtual velocity

$$\boldsymbol{v}=\boldsymbol{u}+\frac{\hbar^2}{4}\frac{(\nabla^2\boldsymbol{s}\cdot\nabla\boldsymbol{s})\times\boldsymbol{\omega}}{\omega^2} \tag{A 18}$$

from (2.37) and (A 15).

REFERENCES

ALFVÉN, H. 1943 On the existence of electromagnetic-hydromagnetic waves. *Ark. Mat. Astron. Fys.* **29**, 1–7.

ALUIE, H. 2009 Hydrodynamic and magnetohydrodynamic turbulence: invariants, cascades, and locality. PhD thesis, Johns Hopkins University, Baltimore, MD.

BRACHET, M. E., MEIRON, D. I., ORSZAG, S. A., NICKEL, B. G., MORF, R. H. & FRISCH, U. 1983 Small-scale structure of the Taylor–Green vortex. *J. Fluid Mech.* **130**, 411–452.

CHEN, S., EYINK, G. L., WAN, M. & XIAO, Z. 2006 Is the Kelvin theorem valid for high Reynolds number turbulence? *Phys. Rev. Lett.* **97**, 144505.

CHERN, A. 2017 Fluid dynamics with incompressible Schrödinger flow. PhD thesis, California Institute of Technology, Pasadena, CA.

CHERN, A., KNÖPPEL, F., PINKALL, U., SCHRÖDER, P. & WEIßMANN, S. 2016 Schrödinger's smoke. *ACM Trans. Graph.* **35**, 77.

CHEVIAKOV, A. F. & OBERLACK, M. 2014 Generalized Ertel's theorem and infinite hierarchies of conserved quantities for three-dimensional time-dependent Euler and Navier–Stokes equations. *J. Fluid Mech.* **760**, 368–386.

CHONG, M. S., PERRY, A. E. & CANTWELL, B. J. 1990 A general classification of three-dimensional flow fields. *Phys. Fluids* A **2**, 765–777.

CHORIN, A. J. 1994 *Vorticity and Turbulence*. Springer.

CHORIN, A. J. & BERNARD, P. S. 1973 Discretization of a vortex sheet, with an example of roll-up. *J. Comput. Phys.* **13**, 423–429.

CLEBSCH, A. 1859 Ueber die Integration der hydrodynamischen Gleichungen. *J. Reine Angew. Math.* **56**, 1–10.

CONSTANTIN, P. 2001 An Eulerian–Lagrangian approach to the Navier–Stokes equations. *Commun. Math. Phys.* **216**, 663–686.

CONSTANTIN, P. & IYER, G. 2008 A stochastic Lagrangian representation of the three-dimensional incompressible Navier–Stokes equations. *Commun. Pure Appl. Maths* **61**, 330–345.

COTTET, G.-H. & KOUMOUTSAKOS, P. 2000 *Vortex Methods: Theory and Practice*. Cambridge University Press.

DAVIDSON, P. A. 2004 *Turbulence: An Introduction for Scientists and Engineers*. Oxford University Press.

ELSÄSSER, W. M. 1950 The hydromagnetic equations. *Phys. Rev.* **79**, 183–183.

ERTEL, H. 1942 Ein neuer hydrodynamischer Wirbelsatz. *Meteorol. Z.* **59**, 271–281.

EYINK, G., VISHNIAC, E., LALESCU, C., ALUIE, H., KANOV, K., BÜRGER, K., BURNS, R., MENEVEAU, C. & SZALAY, A. 2013 Flux-freezing breakdown in high-conductivity magnetohydrodynamic turbulence. *Nature* **497**, 466.

EYINK, G. L. 2009 Stochastic line motion and stochastic flux conservation for nonideal hydromagnetic models. *J. Math. Phys.* **50**, 083102.

GIBBON, J. D., GALANTI, B. & KERR, R. M. 2000 Stretching and compression of vorticity in the 3D Euler equations. In *Turbulence Structure and Vortex Dynamics*, pp. 23–34. Cambridge University Press.

GIBBON, J. D. & HOLM, D. D. 2010 The dynamics of the gradient of potential vorticity. *J. Phys.* A*: Math. Theor.* **43**, 172001.

GOTTLIEB, S. & SHU, C.-W. 1998 Total variation diminishing Runge–Kutta schemes. *Math. Comput.* **67**, 73–85.

GREENE, J. M. 1993 Reconnection of vorticity lines and magnetic lines. *Phys. Fluids* B **5**, 2355.

HALLER, G. 2005 An objective definition of a vortex. *J. Fluid Mech.* **525**, 1–26.

HE, P. & YANG, Y. 2016 Construction of initial vortex-surface fields and Clebsch potentials for flows with high-symmetry using first integrals. *Phys. Fluids* **28**, 037101.

HELMHOLTZ, H. 1858 Uber integrale der hydrodynamischen Gleichungen welche den Wirbel-bewegungen ensprechen. *J. Reine Angew. Math.* **55**, 25–55.

HORNIG, G. & SCHINDLER, K. 1996 Magnetic topology and the problem of its invariant definition. *Phys. Plasmas* **3**, 781.

HOU, T. Y. & LI, R. 2007 Computing nearly singular solutions using pseudo-spectral methods. *J. Comput. Phys.* **226**, 379–397.

HUANG, M., KÜPPER, T. & MASBAUM, N. 1997 Computation of invariant tori by the Fourier methods. *SIAM J. Sci. Comput.* **18**, 918–942.

HUNT, J. C. R., WRAY, A. & MOIN, P. 1988 Eddies, stream, and convergence zones in turbulent flows. In *Center for Turbulence Research Report, Stanford, CA, USA*, pp. 193–208.

JEONG, J. & HUSSAIN, F. 1995 On the identification of a vortex. *J. Fluid Mech.* **285**, 69–94.

JIANG, G. S. & SHU, C.-W. 1996 Efficient implementation of weighted ENO schemes. *J. Comput. Phys.* **126**, 202–228.

KERR, R. M. 1993 Evidence for a singularity of the three-dimensional, incompressible Euler equations. *Phys. Fluids* A **5**, 1725–1746.

KIDA, S. & TAKAOKA, M. 1991 Breakdown of frozen motion of vorticity field and vorticity reconnection. *J. Phys. Soc. Japan* **60**, 2184–2196.

KIDA, S. & TAKAOKA, M. 1994 Vortex reconnection. *Annu. Rev. Fluid Mech.* **26**, 169–189.

LEE, E., BRACHET, M. E., POUQUET, A., ROSENBERG, P. D. & MININNI, D. 2009 Paradigmatic flow for small-scale magnetohydrodynamics: properties of the ideal case and the collision of current sheets. *Phys. Rev.* E **78**, 066401.

LINDSAY, K. & KRASNY, R. 2001 A particle method and adaptive treecode for vortex sheet motion in three-dimensional flow. *J. Comput. Phys.* **172**, 879–907.

MADELUNG, E. 1927 Quantentheorie in hydrodynamischer form. *Z. Phys.* **40**, 322–326.

MAJDA, A. J. & BERTOZZI, A. L. 2001 *Vorticity and Incompressible Flow*. Cambridge University Press.

MOFFATT, H. K. 1969 The degree of knottedness of tangled vortex lines. *J. Fluid Mech.* **35**, 117–129.

MOFFATT, H. K. 1978 *Field Generation in Electrically Conducting Fluids*. Cambridge University Press.

MOFFATT, H. K. 2014 Note on the triad interactions of homogeneous turbulence. *J. Fluid Mech.* **741**, R3.

MOREAU, J. J. 1961 Constantes d'un îlot tourbillonnaire en fluide parfait barotrope. *C. R. Acad. Sci.* **252**, 2810.

MULLIN, T. 2011 Experimental studies of transition to turbulence in a pipe. *Annu. Rev. Fluid Mech.* **43**, 1–24.

NEWCOMB, W. A. 1958 Motion of magnetic lines of force. *Ann. Phys.* **3**, 347–385.

OHKITANI, K. & CONSTANTIN, P. 2003 Numerical study of the Eulerian–Lagrangian formulation of the Navier–Stokes equations. *Phys. Fluids* **15**, 3251–3254.

PENG, N. & YANG, Y. 2018 Effects of the Mach number on the evolution of vortex-surface fields in compressible Taylor–Green flows. *Phys. Rev. Fluids* **3**, 013401.

PRIEST, E. & FORBES, T. 2000 *Magnetic Reconnection: MHD Theory and Applications*. Cambridge University Press.

SAFFMAN, P. G. 1992 *Vortex Dynamics*. Cambridge University Press.

TAYLOR, G. I. & GREEN, A. E. 1937 Mechanism of the production of small eddies from large ones. *Proc. R. Soc. Lond.* A **158**, 499–521.

THOMPSON, W. (LORD KELVIN) 1869 On vortex motion. *Trans. R. Soc. Edinburgh* **25**, 217–260.

TRUESDELL, C. 1954 *The Kinematics of Vorticity*. Indiana University Press.

WU, J. Z. 2018 Vortex definition and 'vortex criteria'. *Sci. China-Phys. Mech. Astron.* **61**, 024731.

WU, J. Z., MA, H. Y. & ZHOU, M. D. 2006 *Vorticity and Vortex Dynamics*. Springer.

XIONG, S. & YANG, Y. 2017 The boundary-constraint method for constructing vortex-surface fields. *J. Comput. Phys.* **339**, 31–45.

YANG, Y. & PULLIN, D. I. 2010 On Lagrangian and vortex-surface fields for flows with Taylor–Green and Kida–Pelz initial conditions. *J. Fluid Mech.* **661**, 446–481.

YANG, Y. & PULLIN, D. I. 2011 Evolution of vortex-surface fields in viscous Taylor–Green and Kida–Pelz flows. *J. Fluid Mech.* **685**, 146–164.

ZHAO, Y., XIONG, S., YANG, Y. & CHEN, S. 2018 Sinuous distortion of vortex surfaces in the lateral growth of turbulent spots. *Phys. Rev. Fluids* **3**, 074701.

ZHAO, Y., YANG, Y. & CHEN, S. 2016 Vortex reconnection in the late transition in channel flow. *J. Fluid Mech.* **802**, R4.

ZHOU, H., YOU, J., XIONG, S., YANG, Y., THÉVENIN, D. & CHEN, S. 2018 Interactions between the premixed flame front and the three-dimensional Taylor–Green vortex. *Proc. Combust. Inst.*; doi:10.1016/j.proci.2018.08.015.

ZHU, J.-Z. 2017 On topological fluid mechanics of non-ideal systems and virtual frozen-in dynamics. arXiv:1702.04447.

ZHU, J.-Z. 2018*a* Local invariants in non-ideal flows of neutral fluids and two-fluid plasmas. *Phys. Fluids* **30**, 037104.

ZHU, J.-Z. 2018*b* Vorticity and helicity decompositions and dynamics with real Schur form of the velocity gradient. *Phys. Fluids* **30**, 031703.

ZHU, J.-Z., YANG, W. & ZHU, G.-Y. 2014 Purely helical absolute equilibria and chirality of (magneto)fluid turbulence. *J. Fluid Mech.* **739**, 479–501.